THE SEARCH FOR CELESTIAL 2.2 MEV NEUTRON CAPTURE LINE

BY

SANDRA J. FLETCHER

B.A., Wesleyan University, 1991

THESIS

Submitted to the University of New Hampshire

in Partial Fulfillment of

the Requirements for the Degree of

Master of Science

in

Physics

December, 1995

This thesis has been examined and approved.

Thesis Director, Mark L. McConnell
Research Assistant Professor of Physics

Robert Leuchtner
Assistant Professor of Physics

James M. Ryan
Associate Professor of Physics

W.Thomas Vestrand
Research Associate of Physics

Date

This thesis is gratefully dedicated to the following:

My parents, whose constant love and support have enabled me to survive another thesis project,

and

Dr. and Mrs. William Crandall, or "Doc and Jeanne", who have made my stay in Durham, New Hampshire very special.

ACKNOWLEDGEMENTS

I feel very fortunate to have had the opportunity to work with the UNH Gamma Ray Observatory Group. Sincere gratitude and admiration go to my thesis advisor Mark McConnell, whose efforts on behalf of this work have been tremendous and much appreciated. Jim Ryan's overall guidance was also appreciated. Tom Vestrand's insights into the scientific theories behind this work were truly helpful. Thanks to Bob Leuchtner for sitting on my committee. The computer gurus of GRO - Tom Milliman, Rita Freuder and John Labonte - have my thanks and my respect for answering many questions. Marc Kippen has been a patient and knowledgable source of all things COMPTEL. For the study of 2.2 MeV, I am also grateful for the insights of Georg Weidenspointer, Gerhard Rank and Cheenu Kappadath. For emotional support throughout the grad school process, I publicly thank Elaine Bennett, Marcus Shappirio and Dr. Dawn Meredith. A final thank you to Jeff Bloch of the Los Alamos National Laboratory, ALEXIS team, for allowing me to finish this project while at LANL.

TABLE OF CONTENTS

LIST OF TABLES

LIST OF FIGURES

ABSTRACT

THE SEARCH FOR CELESTIAL 2.2 MEV NEUTRON CAPTURE LINE

by

Sandra J. Fletcher
University of New Hampshire, December, 1995

The COMPTEL instrument aboard the Compton Gamma Ray Observatory can be used as a gamma ray spectrometer. With its wide field of view (~1 sr) and a 2.2 MeV line sensitivity of 5.5 x 10^{-5} cm^{-2} s^{-1}, COMPTEL covered the entire sky in its first 15 months of operation. Additionally, two more years of observations were combined with the all sky survey to create our basis dataset. As a result, we are able to better the previously reported experimental upper limits by an order of magnitude. We are also able to generate the first ever all sky maps at this energy.

The 2.2 MeV gamma ray is released when a neutron is captured by hydrogen. This line is clearly detected in many solar flares and has yielded insight into the particle acceleration mechanisms in the Sun. Two types of theories have predicted 2.2 MeV lines from X-ray binaries; these predicted line fluxes are on the order of COMPTEL's line sensitivity. Also, both theories predict 2.2 MeV line fluxes which will vary with orbital phases. By binning the data appropriately, we searched for evidence of any orbital trends in the fluxes..

The all sky maps generated at 2.2 MeV are presented. These maps were then examined for evidence of possible sources but only a few were found. Upon further consideration of the statistics of many trials and the level of significance, these 'detections' were deemed marginal at best.

The two theories which have predicted fluxes for Cygnus X-1 and Cygnus X-3 can be examined more closely, since COMPTEL has obtained considerable coverage of both these objects. Despite our sensitivity and the amount of available data, we were only able to report upper limits on the fluxes from these objects. A target list, including 18 additional X-ray binaries, was selected for more detailed analysis. Again, no detections of significant levels were seen in the data. However, since most of these objects had not been examined previously for evidence of 2.2 MeV line emission, we were able to provide new upper limits for these sources. We also produced upper limits for the 2.2 MeV line flux of Cygnus X-1, Cygnus X-3 and Scorpius X-1 which are an order of magnitude more restrictive than earlier experiments.

Finally, the COMPTEL data was examined as a function of orbital phase for both Cygnus X-1 and Cygnus X-3. Unfortunately, no evidence of any enhanced emission was seen in the data. This places some restrictions on the two possible models for the mechanisms behind neutron capture line formation in X-ray binaries.

INTRODUCTION

Gamma ray astronomy is the natural extension of X-ray astronomy to energies greater than 100 keV. Here we shall be concerned with gamma-rays in the 1-10 MeV energy range. At these energies, gamma rays are absorbed in the atmosphere, so that balloons and satellites are required to place detectors high above the atmosphere. These balloon and satellite experiments began in the 1960s and continue to the present day. In addition to the need for elevating the detectors above most of the Earth's atmosphere, an additional complication is the low photon fluxes which are typically encountered. Because of the low signal to noise, accurate knowledge of the background is crucial to successful gamma ray studies.

Physical processes which manifest themselves at these energies include nuclear excitation lines (which also include neutron capture lines), bremsstrahlung emission, Compton scattering, and the decay of neutral pions. While this list is not exhaustive, it gives a flavor for the wide variety of processes which occur in the gamma ray domain.

The celestial objects which are studied at this wavelength are also quite varied. They include, not inclusively, the Crab pulsar, the Galactic Center, active galactic nuclei (AGNs), the Sun (typically solar flares), supernovae, X-ray binary star systems and the mysterious gamma ray bursts.

Gamma ray spectroscopy is an important component of astrophysics. The measurement of nuclear line spectra can be used to study nuclear acceleration processes and the chemical composition of astrophysical objects. For an overview of the current status of gamma ray line research, see Ramaty and Lingenfelter (1995). Successful studies of gamma ray lines have include sola. flares, where lines can be prominent. Measurements of lines in flares have yielded information on elemental abundances on the Sun (e.g., Murphy *et al.*, 1991) as well as particle acceleration mechanisms (e.g., Miller & Viñas 1993).

Regarding studies of non-solar gamma-ray lines, the 1.8 MeV line from the decay of ^{26}Al is thought to trace locations of supernovae (Diehl *et al.*, 1995). Lines in the 3 - 10 MeV energy range have also been observed in the Orion Complex, resulting from high energy particles interacting with the ambient matter (Bloemen *et al.*, 1994). Published theories also predict gamma ray lines at 2.2 MeV to be produced in accreting compact objects, but there have not yet been any convincing, reproducible detections of such radiation. This thesis represents a more detailed search for unshifted 2.2 MeV line emission from non-solar cosmic sources.

Previous satellite missions which have looked for the 2.2 MeV line from various cosmic sources include OSO-7, High Energy Astrophysical Observatory-3 (HEAO-3), and the Solar Maximum Mission (SMM). Several balloon experiments have also been sensitive to 2.2 MeV photon emission. One particularly relevant balloon flight is the JPL June 11, 1979 flight. In April 1991, the Arthur Holly Compton Gamma Ray Observatory (CGRO) was launched. Planned as part of NASA's ambitious Great Observatories Project (which also includes the Hubble Space Telescope), it was later renamed in honor of physicist Arthur Compton. Four instruments were on board: BATSE, OSSE, COMPTEL and EGRET. These instruments scan the sky, covering the energy range from ~10 keV to ~10 GeV.

COMPTEL is a Compton Imaging Telescope, designed to search the sky at energies between 0.75 - 30 MeV. Current projects employing COMPTEL data and involving a search for cosmic line emissions include the mapping of the Galactic Plane at 1.8 MeV (Diehl *et al.*, 1995) and studies of line emission from solar flares. The goal of this work is to use the COMPTEL data to search for sources of <u>unshifted</u> 2.2 MeV line emission.

The motivation to study the 2.2 MeV neutron capture line is two-fold. In the first place, the mechanisms for 2.2 MeV emission have been well studied. These studies have been motivated by the very strong line emission seen in solar flares. In the second place, and more importantly for this work, it has been suggested that this is the most likely line to

be detected from X-ray binary systems (Lingenfelter *et al.*, 1978). In order to generate a 2.2 MeV capture line, one requires two things: 1) a hydrogen target; and 2) a source of neutrons. The most likely target for generating unshifted 2.2 MeV line emission is the companion star. The neutrons may be generated either within the accretion flow (e.g., Guessoum and Dermer 1988) or as the result of some type of particle beam dump somewhere within the binary system (e.g., Vestrand 1990).

CGRO-COMPTEL is an excellent tool to study 2.2 MeV line emission from X-ray binaries systems for several reasons. The line sensitivity at 2.2 MeV is an order of magnitude better than previous instruments. The predicted fluxes from both theoretical scenarios are potentially within COMPTEL's sensitivity range. Also, the long duration of COMPTEL's mission (operational since 1991), coupled with its large field-of-view, has provided considerable exposure to the entire sky. The first 15 months of COMPTEL's life was used to cover the entire sky, so data exists for all areas. Additional observation time has been spent on many XRBs, especially Cygnus X-1 and Cygnus X-3. These data have enabled us to produce the first all sky map at 2.2 MeV, which is one of the principle results of this thesis. In this work, we discuss the theory of X-ray binaries, how COMPTEL works and the results of our 2.2 MeV survey.

CHAPTER I
SCIENTIFIC THEORY

1.1 Review of Binary Star Systems

Binary star systems consist of two stars gravitationally bound to each other in orbit around a common center of mass. This simple definition can be further divided into categories of visual, eclipsing, spectroscopic and spectrum binaries. Visual binaries are those which can be resolved directly, thus requiring a significant angular separation between the two stars. Eclipsing binaries are systems in which the two stars pass in front of each other, from the observer's point of view, causing regular dips in the system's light curve. Spectroscopic binaries are systems in which the Doppler effect shifts emission lines towards the blue and then towards the red as the stars move towards and away from the observer, respectively. Spectrum binaries are a similar class in which two sets of spectral lines are observed, but no Doppler shifting of the lines occurs in either of the star's spectrum. This means that the plane of orbit motion is perpendicular to the line of sight (Bowers & Deeming 1984). Single line spectroscopic binaries (single line because the lines from only one star are seen) which emit either X-rays or gamma rays are suggestive of a compact object (Zel'dovich & Guseynov 1965). This research project investigates a special class of binary systems known as X-ray binaries. This system will be discussed in greater detail below, but the working definition of an X-ray binary system, or XRB, is a binary system from which X-ray emission is detected. Typically, these systems are composed of a compact object in orbit about a main sequence star. Compact objects is a collective term for stars which have reached the end of their evolutionary cycle and have become either white dwarfs, neutron stars, or black holes (Section 1.1.2).

Important characteristics of binary systems include orbital period, period derivative, total mass, scale size, and distance. The orbital period is the amount of time necessary to

complete one full orbit. Features of a binary star system's light curve will occur in a regular, predictable pattern once in each orbital period. The locations of these features can be defined as a function of orbital phase, in which the orbital period is normalized to a length of 1.0. For X-ray binaries, orbital phase 0.0 corresponds to the minimum of the light curve. The period derivative describes how the orbital period is changing with respect to time. Orbital periods can change over time as a result of many things, including mass loss and tidal torque. Both the orbital period and period derivatives are important in performing orbital phase-resolved analysis. The total mass of the system M_* can be calculated from orbital mechanics using Kepler's Third Law

$$a^3 = P^2 \frac{M_*}{M_o} \tag{1.1}$$

where a is the semi-major axis of the orbit in AU (1 AU = 1.496×10^{13} cm), P is the orbital period in years and M_o is the mass of the Sun. Scale size is an important factor in determining if the stars undergo mass transfer and in determining the type of mass transfer. The distance to an object, in conjunction with the emission models, determine the detectability of a source.

1.1.1 Mass Transfer Mechanisms

In general, one can define three different types of binary systems: detached, semi-detached and contact binaries. These are defined based on the position of each stellar surface with respect to the inner Lagrangian point (L1). The inner Lagrangian point is defined as the location between the two stars where a test mass is equally affected by both stars' gravitational fields. The equipotential surface surrounding both stars which has the same gravitational potential as L1 is defined as the Roche lobe. If neither star fills its Roche lobe, the system is considered detached. If only one star fills it's Roche lobe, it is a semi-detached system, and material from one star can be pulled onto the other. A contact

binary occurs when both stars fill their Roche lobes and matter can be freely exchanged between the two stars. Roche lobe overflow tends to be the dominant process for stars below 1.5 solar masses.

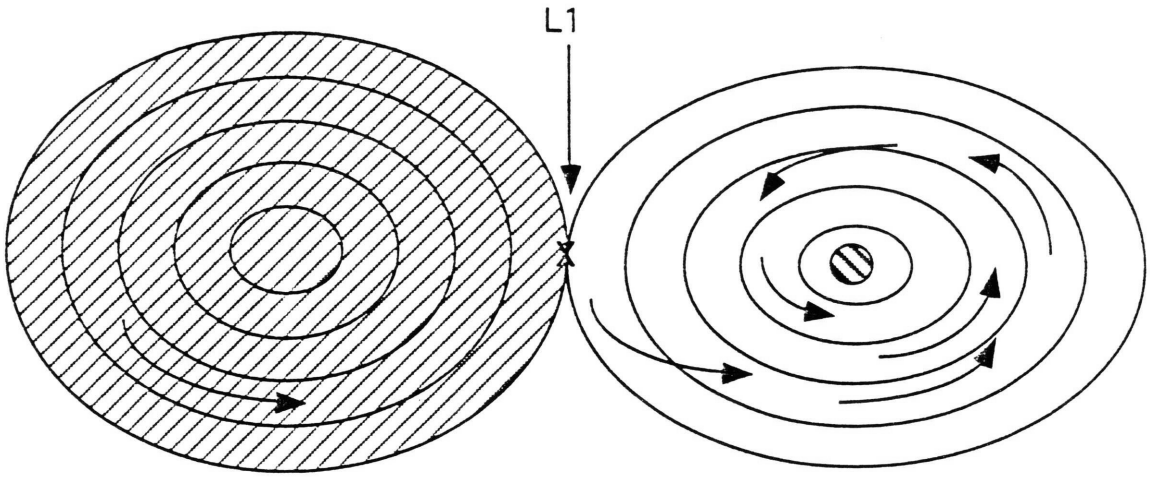

Figure 1.1. An idealized diagram of an XRB, showing the mass transfer point L1 and the accretion disk around the compact object (on the right). Note that the star on the left has filled its Roche Lobe (the outermost circle).

Another possible scenario of mass transfer is stellar wind accretion. While a couple of systems exhibit both types of mass transfer, wind accretion is the important mechanism for companion stars of spectral type O or Be (White *et al.*, 1995). Since wind accretion requires younger, more massive stars with very strong stellar winds, this process is applicable for binaries in which the mass of the companion is greater than about 8 solar masses. Some fraction of the material in the stellar wind is captured by the companion's gravitational field.

As the material from one star is captured by the gravitational field of the other, it does not necessarily fall directly onto the other star's surface. In Roche lobe overflow, the angular momentum which is imparted to the matter at L1 causes the matter to swirl into a thin accretion disk. In the case of wind driven accretion, the flow starts out as a radial flow from the shedding star, but it may be slightly focused through the Lagrangian point. Depending on the extent of this focusing effect, the captured material may or may not form an accretion disk. In either case, as the gravitational potential energy is transferred to

kinetic energy within the disk, the temperature increases dramatically. Theoretical predictions of the ion temperature in the inner region of the disk around a black hole can reach 10^{12} K (Aharonian & Sunyaev 1986) or 100 MeV. The corresponding electron temperature is ~10^9 K ($\geq$ 100 keV). More typical temperatures of the accretion disk are approximately ~ 10^6 - 10^7 K (100 eV to a few keV), which is considered the X-ray region of the energy spectrum. At such temperatures, luminosities can be high and therefore easily detected by X-ray instruments.

1.1.2 White Dwarfs, Neutron Stars and Black Holes

In X-ray binaries, one of the two stars is typically a compact object, i.e., a white dwarf, a neutron star or a black hole. These stars have evolved off the main sequence after depleting their nuclear fuel resources and so they can no longer support themselves by thermal pressure. Since white dwarfs are less massive, the accretion process in a white dwarf system tends to radiate more in the UV and soft X-ray ranges. The greater mass of neutron stars and black holes allow for a greater kinetic energy transfer to the infalling material, resulting in hard X-ray and possibly gamma ray emission. Usually, the neutron star or black hole itself cannot be seen optically and its detection relies upon the accretion disk X-ray emission.

Table 1.1. Compact objects and their properties. Note the black hole radius is the Schwartzchild radius.

OBJECT	RADIUS (km)	CORE MASS (solar mass $M_\odot$)	INTERNAL PRESSURE
white dwarf	~ 5000	< 1.4	electron degeneracy
neutron star	~ 10	1.4 - 3	neutron degeneracy
black hole	= 2.96 ($M_* / M_\odot$)	> 3	none (total collapse)

White dwarfs are the end stage for stars which are like our own Sun. On average, the stellar cores are of one solar mass and are Earth-sized. Their maximum mass of 1.4 solar masses is known as the Chandrasekhar limit. After completing the main sequence

part of their lives, nuclear fusion no longer balances the gravitational force and the star contracts. This contraction is ultimately halted by electron degeneracy pressure. This quantum mechanical condition means that the uncertainty of the electrons' momentum results in a wide spread of velocities. The high velocities generate a pressure known as electron degeneracy pressure, which prevents the star's further collapse (Shu 1982). X-ray binaries with white dwarfs as the compact object are sometimes called cataclysmic variables (CVs).

Neutron stars are the end stages for stellar cores which are more massive than the Chandrasekhar limit but less than ~3 solar masses. As a result of the more energetic collapse, the electrons which would have created electron degeneracy pressure undergo inverse β decay. When the protons and electrons are crushed together, a neutron gas is formed and results in neutron degeneracy (Longair 1994). These objects also have strong magnetic fields on the order of 10^{12} Gauss (based on cyclotron line measurements from pulsars) (White *et al.*, 1995).

For a core mass greater than 3 solar masses, neutron degeneracy is insufficient to prevent gravitational collapse. The stellar core continues to collapse to a singularity, where the gravitational field strength becomes so great that even light cannot escape. Since light is captured by this singularity and hence no emission from it is expected, this object is called a black hole. While the theoretical construct is accepted in the astronomical community, experimental 'evidence' of black holes has historically been difficult to obtain. The crucial evidence from orbital dynamics is that the unseen object in an XRB has a mass greater than the 3 solar mass limit of the neutron star. The first experimental evidence of a black hole came in 1972 with the discovery of Cygnus X-1 (for a review, see Tanaka & Lewin 1995). In the past several years, soft X-ray transients have become prime black hole candidates. More recently, experimental evidence of supermassive (~10^6 solar masses) black holes in active galactic nuclei (AGNs) has been mounting (Miyosji *et al.*, 1995).

1.1.3 The Companion Star

In an X-ray binary system, the companion is typically a normal, main sequence star. X-ray binaries are separated into two categories depending on the mass of the companion. If the companion star is of ~ 2 solar masses or less, the system is considered a low mass X-ray binary (LMXB). In this case, the companion stars tend to be older stars (low mass stars evolve more slowly than higher mass stars) and, as such, tend to be located in the Galactic Bulge. Roche lobe overflow is the dominant mass transfer mechanism for these objects.

The second category is a high mass X-ray binary (HMXB). These systems are composed of a compact object and a much more massive and luminous companion, typically a late O or early B type star. As these are a younger population (higher mass means faster evolution), they lie along the Galactic plane. Because the massive companions typically have strong stellar winds, wind driven accretion can be important.

1.2 The 2.2 MeV Neutron Capture Line

When thermalized neutrons are captured by ambient hydrogen or protons to form deuterium, the binding energy of 2.223 MeV is released as a gamma ray. The reaction involved is the following:

$$n + H^1 \rightarrow d + \gamma_{2.2\,MeV} \tag{1.2}$$

Whether or not this capture process will occur before the neutron decays (with a lifetime of 918 seconds) depends on the proton density of the target. The neutron must thermalize in order to capture, since the cross-section of neutron-proton elastic scattering will dominate at high velocities. The cross-section for neutron-proton capture can be expressed as

$$\sigma_{cap} = \frac{1}{n_p v_n t_{cap}} \tag{1.3}$$

where v_n is the velocity of the neutron, t_{cap} is the capture timescale and n_p is the proton density. The capture cross-section can also be written

$$\sigma_{cap} = \frac{\sigma_o}{v_n} \tag{1.4}$$

where $\sigma_o = 7.3 \times 10^{-20}$ cm^3 s^{-1} for the neutron-proton capture. Requiring that t_{cap} is less than 918 seconds and solving equation 1.3 for n_p, one can see that if the proton density exceeds 1.5×10^{16} cm^{-3}, then neutron capture will be significant.

1.2.1 Solar Flares and Neutron Capture

The neutron capture line has been clearly detected in many solar flares by several different instruments, including OSO-7, HEAO-3, SMM and CGRO. COMPTEL's detection of the June 11th, 1991 flare had prominent line structure from several elements, including a strong 2.2 MeV line. Wang and Ramaty (1974) performed detailed Monte Carlo simulations of neutron behavior in solar flares. They found a significant number of neutrons would be aimed back towards the solar surface. These neutrons thermalize and capture on the hydrogen in the photosphere, creating 2.2 MeV photons. Some fraction of these photons, if not attenuated in the solar photosphere, would then be detected at Earth. From solar flare 2.2 MeV measurements, we can gain insight into the particle acceleration mechanism in the Sun. This motivates the search for cosmic 2.2 MeV line sources where the line detection may provide information about the energetic particle processes taking place at the source.

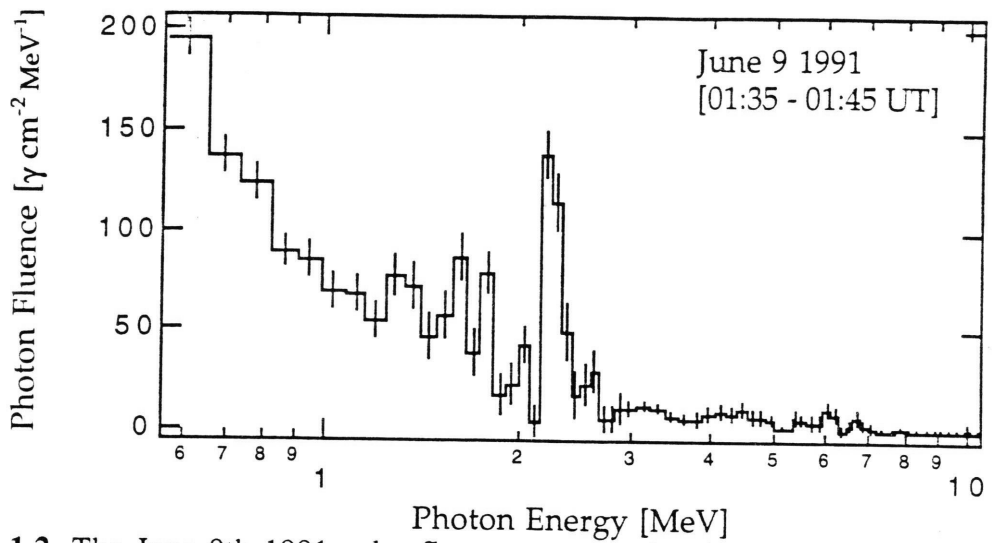

Figure 1.2. The June 9th 1991 solar flare spectrum, showing strong emission lines, especially the 2.2 MeV line [from Suleiman 1995].

1.2.2 Generation of 2.2 MeV Line Emission in X-ray Binaries

While 2.2 MeV line emission is clearly detected in solar flares, we want to review the requirements for generation of the neutron capture line in X-ray binary systems. In order to generate a 2.2 MeV capture line, one requires two things: 1) a hydrogen target; and 2) a source of neutrons.

Within a compact binary system, there will be two principle sites for neutron capture, i.e., regions in which there exists an ample supply of ambient hydrogen. The first such site is in the accretion flow itself. Neutron capture which takes place in this region, however, will likely lead to gravitationally redshifted line emission, especially if the capture takes place in the inner part of the accretion disk. Since this study concentrates on unshifted line emission, we will be most interested in the neutron capture process as it takes place elsewhere in the system. The second possible site of neutron capture is in the atmosphere of the companion star. The (typically) main sequence companion star contains ample hydrogen. Here, the resulting line emission would be immune to any gravitational redshifts.

Within the context of neutron capture on the companion star, there are two possible sources of neutrons. The first is the accretion disk itself, which may be sufficiently hot to generate neutrons which subsequently escape to interact in the companion star. A second alternative is that the neutrons may be generated in the companion star itself as the result of a particle beam dump, much like a solar flare. We consider both such possibilities below.

It should be noted that, in order for the line emission to be detectable, it must be of the same order as the continuum emission. For the energy range near 2.2 MeV, the continuum emission is most likely to originate from electron bremsstrahlung so the condition of $E_e < 1$ MeV $< E_{ion}$ must be met (Lingenfelter *et al.*, 1978). This translates to a temperature restriction of $T_e < 10^{10}$ K $< T_{ion}$. As we will see below, this restriction can be met in the context of two temperature accretion disk plasmas.

1.2.3 Neutron Production in X-ray Binary Systems In An Accretion Disk

One site of neutron production in XRBs has been extensively studied - the accretion disk. Depending on the composition of the companion star, the infalling material consists primarily of hydrogen and helium, with the addition of some light metals (such as carbon, nitrogen and oxygen). As this matter forms an accretion disk, the gravitational potential energy is transformed into kinetic energy. Heating and cooling within this plasma affects different particles in different ways. As the matter falls into the deep potential well of the compact object, more energy is imparted to the heavier particles (protons, ions) than the lighter particles (electrons). From the outset, a two temperature plasma is formed. As mentioned previously, a neutron star can certainly give a proton more than 1 MeV of energy. This difference in temperatures is maintained because elastic Coulomb scattering is not enough to equalize their temperatures (Shapiro, Lightman & Eardley 1976, Higdon & Lingenfelter 1977). The electrons are cooled more rapidly than the ions as a result of Comptonization (Aharonian & Sunyaev 1984), which further enhances the temperature

difference. Aharonian and Sunyaev (1984) discuss the effects of this two-temperature plasma on the 2.223 MeV line emission (assuming solar type abundances of ions).

Since accretion is an efficient ($\varepsilon \sim 10\%$) manner for energy conversion, the plasma temperature predicted ranges from electron temperatures of ~ 10^9 K to ion temperatures of ~ 10^{11} K. Assuming typical neutron star properties (1.5 solar masses, 10 km radius), a proton falling in to the surface can release energies in excess of ~10 MeV (or 10^{11} K). In this temperature regime, spallation, or break up reactions, become important. For solar abundances, neutron production is driven by the inelastic collisions of protons with nuclei of ^{4}He (Aharonian & Sunyaev 1984). The principle reactions involved are

$$p + He^4 \rightarrow \begin{array}{l} He^3 + d \\ He^3 + p + n \\ H^3 + 2p \\ 2d + p \\ d + n + p. \end{array} \qquad (1.5\ a\text{-}e)$$

Both deuterium and He^3 can eventually form neutrons by subsequent breakup reactions.

Guessoum and Dermer (1988) further refined Aharonian and Sunyaev's spallation analysis by using time-dependent abundance factors which incorporated the effects of the spallation reactions. Guessoum and Dermer examined the particular case of Cygnus X-1, a 10 solar mass black hole. They assumed a plasma consisting of hydrogen and helium. In this case, they found that most neutrons, which are created in the spallation of He^4, leave the hot ion plasma. This is due to two factors, 1) neutrons are not confined by magnetic fields in the accretion disk; and 2) neutrons can have sufficient energy to escape the disk at ion temperatures greater than 5 MeV (Aharonian & Sunyaev 1984). Since Cygnus X-1 is a close binary system (orbital period of 5.6 days), the neutrons have an opportunity to escape the accretion disk, thermalize within the comapnion star's atmosphere and then undergo neutron capture before the neutrons decay. The predicted values for the 2.2 MeV flux are dependent on the capture probability of the neutrons (largely a geometrical factor, based on the angular size of the companion star as seen from the neutron production site) and also on

the initial ion temperature of the plasma. The resulting flux levels range from 2.8 x 10^{-6} to 7.2 x 10^{-5} cm^{-2} s^{-1} (Guessoum & Dermer 1988). This range is within the line sensitivity of COMPTEL of 5.9 x 10^{-5} cm^{-2} s^{-1} for a two week observation.

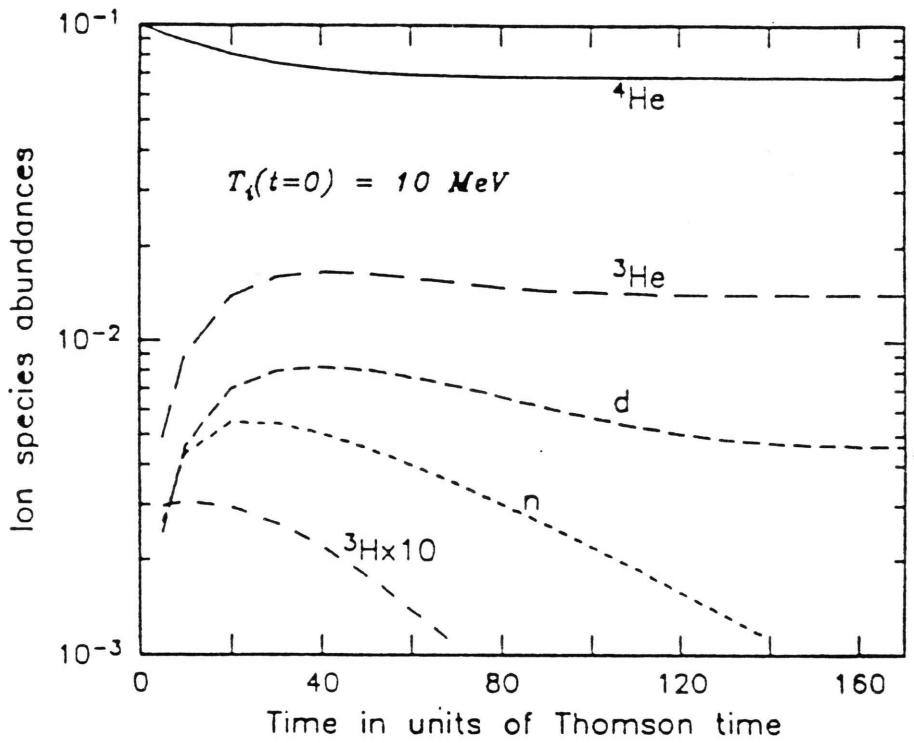

Figure 1.3. Neutron and other elemantal abundances as a function of Thomson time (1 Thomson unit = 3.3 x 10^{-4}s). Note the decline of neutrons. [From Guessoum & Dermer 1988].

These flux estimates are averaged over the orbital period. For neutron capture taking place on the companion star, we expect that the emission would vary with the orbital phase. The 2.2 MeV line flux should be zero when the compact object is behind the companion star (relative to the observer) and then be a maximum when the compact object is directly between the observer and the companion star, so that the illuminated face of the companion star is visible to the observer.

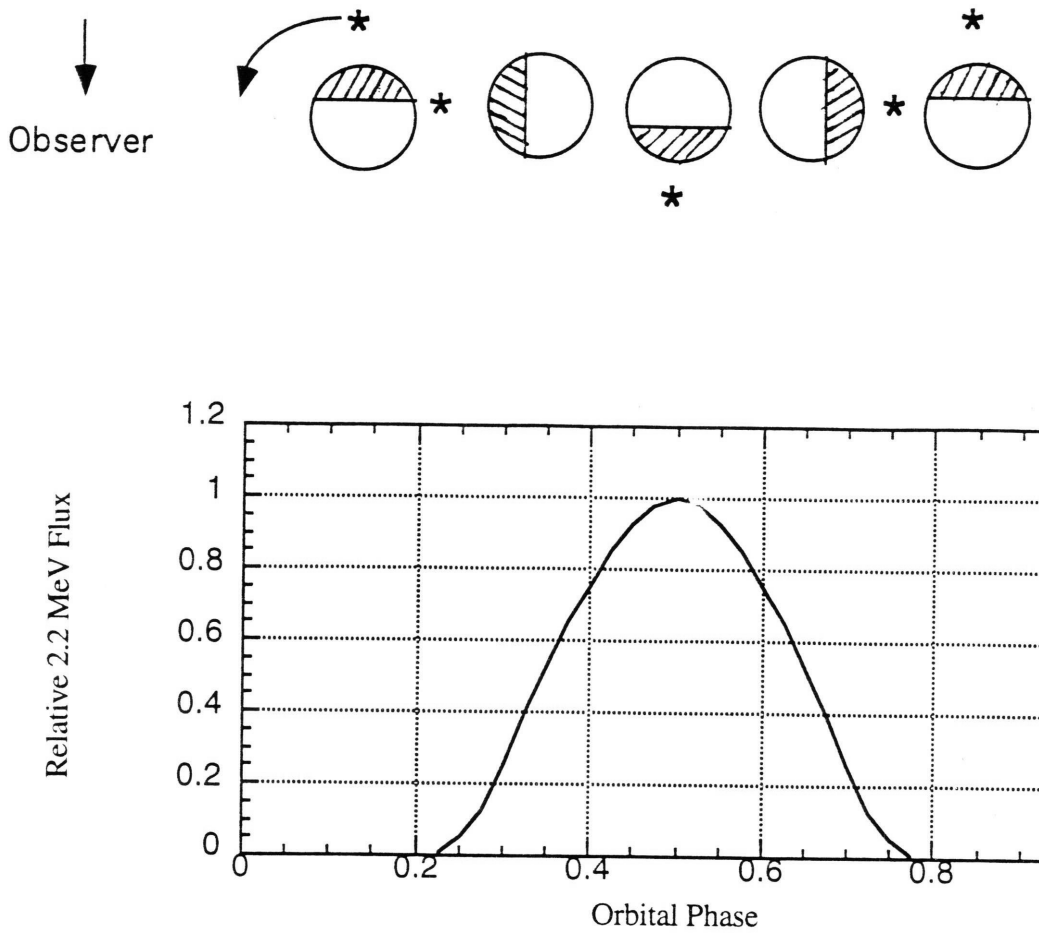

Figure 1.4. A diagram of an X-ray binary system with a graph of relative 2.2 MeV flux showing how the emission would vary with orbital phase.

If 2.2 MeV line emission is detected by COMPTEL, this would provide very strong evidence for the two temperature plasma model (Guessoum & Dermer 1988). Also it is an important test for neutron production and subsequent escape from the accretion disk (Aharonian & Sunyaev 1984).

1.2.4 Neutron Production in a Beam Dump Model

Another mechanism for the neutron production (and subsequent capture) is based on the observational evidence for TeV photon emission (see Weekes 1992 for a review). TeV photon emission is considered to be very high energy (VHE) gamma rays ($>10^{15}$ eV). Unlike the MeV energy range, these energetic photons can be detected by instruments on

Earth, albeit on mountain tops. The high energy photons induce electromagnetic air showers when they enter the Earth's atmosphere. The photons annihilate into electron and positron pairs, which radiate via bremsstrahlung. The radiated gamma rays can themselves undergo electron/positron production. This process will continue to "cascade" until there is no longer sufficient energy to overcome the pair production threshold. While the gamma rays are being absorbed, the particles are moving faster than the speed of light in the atmosphere. The shock waves generated by the electron's passage create a cone of bluish light, called Cerenkov radiation. By collecting this visible signal using arrays of optical collectors, the emission can be traced back to a source location in the sky.

The Whipple Observatory team has published results from the Crab pulsar, which are significant at a 20 σ level (Vacanti *et al.*, 1991). Observations of several other sources, however, have proven to be more controversial (Weekes 1992) as the observing technique is fraught with difficulties. The issue of the detection of Cygnus X-3 and other XRBs is still open to scientific debate (Bidaud-Bonnet & Chardin 1988). Among the concerns are detections in one telescope but not in another and detections in different instruments but with differing orbital parameters (Weekes 1992). Also, there have been no recent reported detections at these extremely high energies.

Vestrand (1990) suggests that the non-thermal particle acceleration mechanism which would be responsible for the TeV emission might also generate 2.2 MeV line mission in X-ray binaries with small scale sizes. Protons accelerated via pulsar or shock mechanisms may provide an accelerated particle beam which can interact with material elsewhere in the system. This process follows the solar flare 2.2 MeV line production, where the flare accelerates the ions, which then interact in the solar atmosphere. Since 2.2 MeV line emission is very strong in solar flares (see Section 1.2.1), this process has been studied in detail (e.g., Murphy & Ramaty 1985, Hua & Lingenfelter 1987, and Vestrand 1990). Following the solar flare analogy, Vestrand suggests that 2.2 MeV line emission can be generated in either of two ways: 1) the energetic protons strike the companion star's

surface, where neutrons are produced, thermalized and captured; or 2) the energetic protons generate neutrons at an acceleration region away from the companion star, and the neutrons "leak" from the region, impinging on the companion star.

Vestrand expresses the peak line flux of 2.2 MeV line emission for Cygnus X-3 as

$$F_{2.2\,MeV} \leq 2x10^{-4}\left(\frac{f_{2.2}}{0.4}\right)\left(\frac{\varepsilon_n}{0.1}\right)\left(\frac{\Omega_s}{2\pi}\right)\left(\frac{E_n}{10\ MeV}\right)^{-1}\left(\frac{L_p}{10^{39}\ erg/s}\right)\left(\frac{D}{11.6\ kpc}\right)^{-2}\frac{photons}{cm^2\ s} \tag{1.6}$$

where $f_{2.2}$ is the fraction of energetic neutrons which are thermalized and captured before they decay, ε_n is the efficiency of the accelerating process, Ω_s is the solid angle subtended by the companion star's surface, E_n is the neutron energy spectrum, L_p is the proton luminosity and D is the distance to the object. The two most uncertain parameters are the neutron spectrum (as characterized by the average neutron energy, E_n) and the proton luminosity L_p. A value of 10 MeV was chosen for E_n as this optimizes the probability that the 2.2 MeV photon can be produced and that it can subsequently escape the star's surface without being attenuated. A higher neutron energy will produce a 2.2 MeV photon too deeply in the star's surface so it won't be able to escape as a 2.2 MeV photon. The parameter L_p was chosen to be consistent with the proton luminosity of the TeV emission reports of Cygnus X-3. This upper limit for the 2.2 MeV line flux is well within COMPTEL's line sensitivity. As with the model of Guessoum and Dermer, this line emission should also be orbital phase-dependent (see Figure 1.4), with the maximum detection at ~0.5 phase.

1.2.5 Previous Experimental Results

During a JPL balloon flight on June 10, 1974, a flare-like event was observed (Jacobson *et al.*, 1978). Lasting 20 minutes, four gamma ray lines (with no associated continuum) were detected at 0.41 MeV, 1.79 MeV, 2.22 MeV and 5.95 MeV. Since this

was a collimated detector with no imaging capabilities, the ability of the experiment to determine the location of the source was poor. Included in the field of view were Mercury and Saturn, supernova remnant IC443 and pulsar 0611+22 and the high energy gamma ray source CG195+5 (the Geminga pulsar). The Crab pulsar and the Sun were on the edge of the field of view. The lines at 0.41 MeV and 1.79 MeV are consistent with gravitationally redshifted 0.511 MeV and 2.22 MeV lines, respectively, assuming that they originate near the surface of a 1.2 M_O neutron star. It has been suggested that the 1.79 MeV emission was generated by neutron capture onto hydrogen close to the neutron star's surface, while additional 2.2 MeV emission was created in a much weaker gravitational field (Lingenfelter & Ramaty 1978) The reported fluxes of the 1.79 and 2.22 MeV lines are given in Table 1.2.

Table 1.2. June 11, 1974 transient 2.2 MeV fluxes [from Jacobson *et al*, 1974]

LINE ENERGY (MeV)	FLUX (photons / cm^2 s)
1.7897 (± 0.0060)	3.15 (± 0.74) x 10^{-2}
2.2186 (± 0.0063)	3.15 (± 0.74) x 10^{-2}

If this is a real cosmic source, then it would represent the first (and only) detection of 2.2 MeV emission from an object other than the Sun. Unfortunately, no one has been able to determine a counterpart to this transient object, so the source of this emission remains a mystery.

HEAO-3, part of the High Energy Astrophysical Observatory series, was designed to search for narrow line emission from cosmic sources. A measurement of the 2.2 MeV line flux from Scorpius X-1 was performed based on data collected from January 25 to March 25, 1980. For a total effective observing time of 10^5 s, they calculated a 3σ upper limit on the 2.2 MeV line flux. Their result was $F_{3\sigma} < 9.1 \times 10^{-4}$ cm^{-2} s^{-1} (Bhattacharya *et al.*, 1991).

Upper limits on the 2.2 MeV flux levels from several sources came from the Solar Maximum Mission Gamma Ray Spectrometer (SMM-GRS). Using data accumulated from

1980 to 1989, Harris and Share (1991) searched for 2.2 MeV line emission from Cygnus X-1, Cygnus X-3 and Scorpius X-1 when these objects were within the SMM field of view. They looked for increases in the count rate around 2.2 MeV as these objects transited the SMM aperture. Therefore, these upper limits are for time averaged, steady emission. The data was binned into 3-day long intervals, so Cygnus X-1's emission might have been eclipsed during its 5.6 day orbital period. Both Cygnus X-3 and Scorpius X-1 have orbital periods less than the 3-day binning, so occultation effects could reasonably be ignored. Their results are shown in Table 1.3.

Table 1.3. Solar Maximum Mission 2.2 MeV line fluxes [from Harris & Share 1991]

SOURCE	LINE FLUX (photons / cm^2 s)	3 σ UPPER LIMIT (photons / cm^2 s)
Cyg X-1 (occulted)	$3.3 \pm 6.2 \times 10^{-5}$	2.2×10^{-4}
Cyg X-1 (unocculted)	$2.1 \pm 3.4 \times 10^{-5}$	1.2×10^{-4}
Cyg X-3	$2.1 \pm 3.4 \times 10^{-5}$	1.2×10^{-4}
Sco X-1	$0.4 \pm 3.1 \times 10^{-5}$	1.0×10^{-4}

1.3 The Target List

The COMPTEL all-sky survey permits, for the first time, a search for 2.2 MeV line emission from a large number of candidate sources. We have selected a set of twenty objects, representative of both LMXBs and HMXBs, for quantitative study for 2.2 MeV line emission (see Table 1.4). Cygnus X-1, Cygnus X-3 and Scorpius X-1 were chosen as upper limits were already published for these objects and COMPTEL would be able to improve these values by an order of magnitude. Additionally, specific models predicted potentially observable 2.2 MeV line emission from Cygnus X-1 and Cygnus X-3. The other objects were selected on the basis of their known characteristics and the likelihood that they might also be detectable emitters of 2.2 MeV line emission. For example, our target list includes all known stellar mass black hole candidates (e.g., Tanaka & Lewin 1995). It also includes several sources for which there are reports of TeV emission (Weekes 1992).

TABLE 1.4. Target list for COMPTEL study. (Data from van Paradijs (1995).

Name	l (deg)	b (deg)	Class	Distance (kpc)	Period (days)	Scale size (x 10^{11} cm)	Companion Star
Cyg X-1	71.3	3.1	HMXRB	2.5	5.6	9.2	V1357 Cyg
Cyg X-3	79.9	0.7	HMXRB	11	0.2	1.0	V1521 Cyg
2000+251	63.4	-3.1	LMXRB Transient	2	0.3	1.3	QZ Vul
2023+338	73.2	-2.2	LMXRB Transient	2	6.5	10.2	V404 Cyg
LMC X-1	280.2	-31.5	HMXRB	55	4.2	7.6	star 32
LMC X-3	273.6	-32.1	HMXRB	55	1.7	4.2	star 1
CAL 83	278.6	-31.3	LMXRB		1.0	1.0	star V
GX 339-4	338.9	-4.3	LMXRB Transient	10	0.6	2.1	V821 Ara
SS 433	39.7	-2.3	HMXRB	3	13.1	13.1	V1343 Aql
Aql X-1	35.7	-4.1	LMXRB Transient, Burst		0.8	2.5	V1333 Aql
Cen X-3	292.0	0.9	HMXRB	5 - 10	2.1	4.8	V779 Cen
N Mus 1991	295.0	-7.1	LMXRB	1.4	0.4	1.6	
Her X-1	58.2	37.5	LMXRB Pulsar	5	1.7	4.2	HZ Her
0115+63	125.9	1.0	LMXRB Transient, Pulsar	3	24.3	24.6	V635 Cas
Vela X-1	263.1	3.9	HMXRB	1.5	9.0	12.7	GP Vel
CAL 87	281.8	-3.1	LMXRB	55	0.4	1.6	
Sco X-1	359.1	23.8	LMXRB	0.7	0.8	2.5	V818 Sco
06200+00	210.0	-6.5	LMXRB Transient	0.87	0.3	1.3	V616 Mon
1755-338	357.2	-4.9	LMXRB		0.2	1.0	V4134 Sgr
Cir X-1	322.1	0.0	LMXRB Transient, Burst	10	16.6	19.1	BR CIR

CHAPTER II

CGRO-COMPTEL AND DATA ANALYSIS

2.1 The Compton Gamma Ray Observatory

The Compton Gamma Ray Observatory (CGRO) was launched aboard the Space Shuttle Atlantis on April 5, 1991. Placed in a circular Earth orbit at an altitude of 450 km and an inclination of 28.5 degrees, it completes an orbit approximately every 90 minutes. CGRO consists of four instruments, each providing a different capability and collectively covering the energy range of 20 keV to 10 GeV. They are known as the Burst and Transient Source Experiment (or BATSE, an all sky monitor covering 20 keV to 10 MeV), the Oriented Scintillation Spectrometer Experiment (or OSSE, a collimated array covering 50 keV to 10 MeV), the Compton Imaging Telescope (also known as COMPTEL, which covers 0.75 MeV to 30 MeV), and Energetic Gamma Ray Experiment Telescope (or EGRET, an imaging telescope which covers the energy range between 50 MeV and 10 GeV).

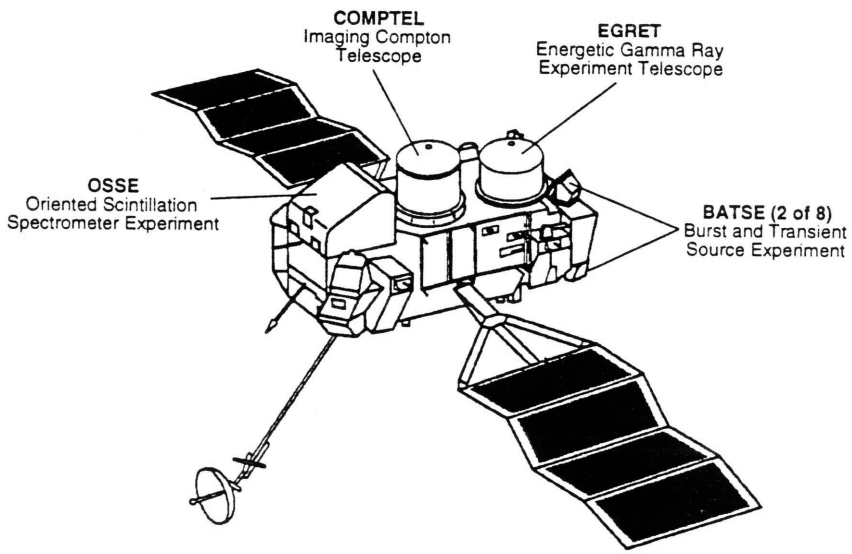

Figure 2.1. Schematic of the Compton Gamma Ray Observatory (CGRO).

The 2.2 MeV emission lies within the energy ranges of both COMPTEL and OSSE, so it is beneficial to compare the two instruments. COMPTEL is an imaging telescope with a wide field of view of ~1 sr . For a 14 day observation, COMPTEL has a 2.2 MeV line sensitivity of ~5.5 x 10^{-5} cm^{-2} s^{-1}. With its large field of view, COMPTEL has completed the first ever all-sky survey at MeV energies. OSSE, on the other hand, has four passively collimated NaI scintillators, a field of view of 3.8° by 11° and a somewhat poorer line sensitivity which ranges from ~ 10 - 12 x 10^{-5} cm^{-2} s^{-1} (Johnson *et al.*, 1989). During its lifetime, OSSE has covered a comparably small fraction of the sky. Therefore, COMPTEL is the better instrument with which to search for 2.2 MeV emission.

The COMPTON Gamma Ray Observatory's operational life is divided into several *phases*, based primarily on the NASA funding cycle. The first phase provided coverage of the entire sky and lasted for 15 months. The following phases (2,3, etc.) are each of approximately one year duration and consist of target specific observations. An up-to-date breakdown of these phases is given in Table 2.1.

Table 2.1 The COMPTON Gamma Ray Observatory Mission Phases

Observational Phase	Start Date	End date
1	17 June 1991	17 November 1992
2	17 November 1992	17 August 1993
3	17 August 1993	4 October 1994
4	4 October 1994	3 October 1995
5	3 October 1995	14 October 1996

Within each phase are several *viewing periods*. Each viewing period is defined by a continuous observation with a single telescope pointing direction, which typically lasts for two weeks. When COMPTEL's pointing direction changes to look at a different object, a new viewing period begins.

2.2 The Compton Imaging Telescope (COMPTEL)

COMPTEL is an imaging telescope which uses the Compton scattering process for imaging gamma ray photons in the 0.75-30 MeV energy range (see Figure 2.2). For the

definitive explanation of the COMPTEL instrument, see Schönfelder *et al.* (1993). An abbreviated discussion is presented here. COMPTEL consists of two detectors layers, D1 and D2, placed 1.5m apart. Each detector layer is surrounded by plastic scintillators, or "veto domes", to aid in rejecting charged particle events. The first detector layer (D1) consists of an array of seven modules, each of which consists of low Z liquid (NE213A) scintillator. This upper detector is designed to maximize the probability of an incoming photon scattering once off of an electron in the scintillator. A measurement of pulse shape (PSD) is made in the D1 layer to separate gamma ray events from neutron-induced events (see Figure 2.3.a). The photon's energy loss and the location of the collision (in the x,y plane only) are also measured in D1.

In the case of an ideal event, the photon's energy loss is totally absorbed in D1 and the scattered photon travels to the lower detector layer (D2). The D2 layer is composed of 14 high Z, NaI(T1) scintillator modules. The second detector is designed to stop the photon, so that the remaining photon energy, as well as its interaction location (again, in the x-y plane only), is measured. The time of flight (ToF) measurements, which measure the time-of-flight between D1 and D2, are used to select only forward moving events (events which begin in D1 and go to D2) (see Figure 2.3.b). An upper limit is also placed on the ToF to insure that events measured in D1 and D2 are from the same photon, rather than two unrelated events. Finally, each event is time tagged. So for each photon event, the following information is recorded:

1. the energy loss in D1 (E1)
2. the interaction position in D1 (x,y only)
3. the pulse shape in D1 (PSD)
4. the energy loss in D2 (E2)
5. the interaction position in D2 (x,y only)
6. the time of flight between D1 and D2 (ToF, ~1ns resolution)
7. the time of the event (125 μsec resolution)

Parameters 1, 2, 4 and 5 serve to define the event kinematics and parameters 3 and 6 are useful in discerning background events from source events.

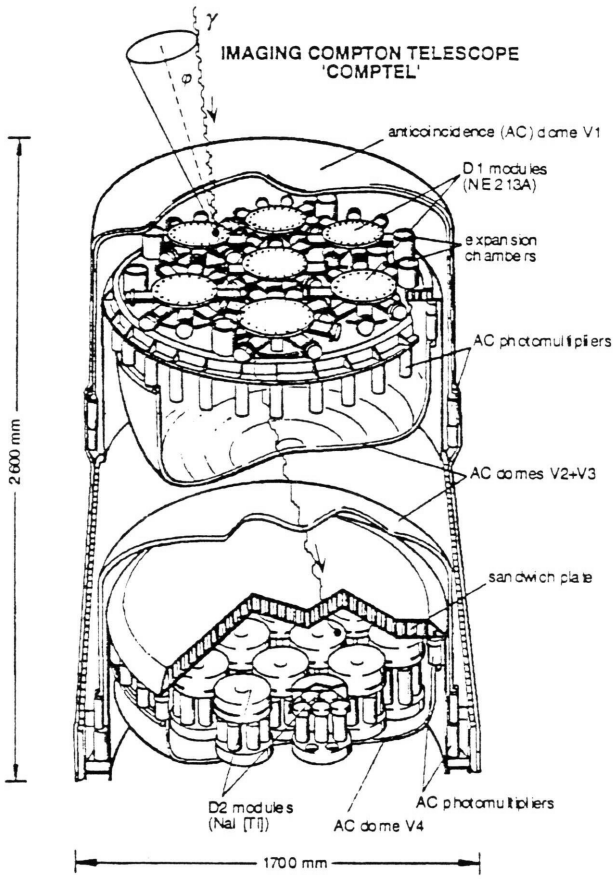

Figure 2.2. Diagram of the COMPTEL instrument, showing an ideal telescope event.

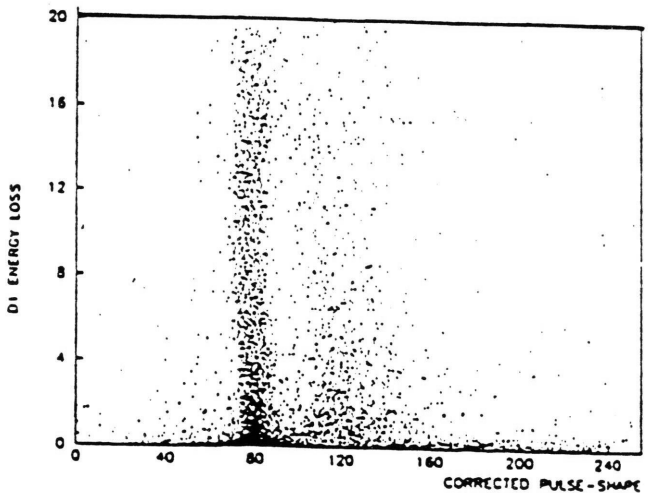

Figure 2.3. a) A sample PSD (Pulse Shape Discrimination) spectrum, based on in-flight data. Gamma ray events are centered around channel 80 while neutron events are centered around 120. By selecting events in channel 110 or below, many neutron events are eliminated from the data.

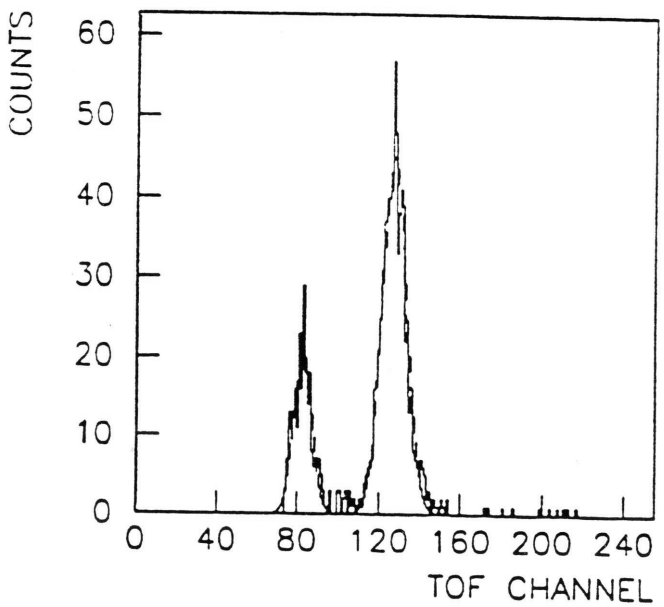

Figure 2.3 b) A sample ToF (Time of Flight) spectrum, based on in-flight data. Forward moving events (events interacting in D1 first) are centered around channel 120. Backward scattered events (events interacting in D2 first) are centered around channel 80. Slower moving neutron events are typically found above channel 120.

Two ^{60}Co gamma ray sources are located on the sides of COMPTEL, equidistant between D1 and D2. In each case, the ^{60}Co is embedded in plastic scintillator. Since each photon decay is accompanied by an associated beta particle, the beta particle is detected in the plastic scintillator (with >99% efficiency). This results in an electronic 'tagging' of each ^{60}Co photon. These events are used for the in-flight gain corrections of the PMTs in the detector modules. These adjustments are necessary to compensate for several time varying effects which may affect PMT pulse heights.

As mentioned previously, an ideal event is one in which the energy imparted to the electron is fully absorbed in the D1 detector layer and the energy of the scattered photon is completely absorbed in D2. The angle ϕ_{GEO} is defined as the true angle between the source of the gamma ray and its scattered trajectory (the line from the interaction site in D2 to the interaction site in D1). For each event, we define an estimated scatter angle ϕ (which we call $\bar{\phi}$) as

$$\cos(\bar{\phi}) = 1 - m_o c^2 \left[\frac{1}{E_1} - \frac{1}{(E_1+E_2)} \right] \qquad (2.1)$$

where $m_o c^2$ is the electron rest energy and E_1 and E_2 are the energies measured in D1 and D2, respectively. In the case of an ideal event, $\bar{\phi}$ represents (to within measurement errors) a measure of the true scatter angle (ϕ_{GEO}). The value of $\bar{\phi}$ is also used to define the radius of a circle whose center corresponds to the direction of the event scatter vector (χ,ψ). Roughly speaking, given enough events, the intersection of all of these "event circles" can be used to determine a source location (see Figure 2.4).

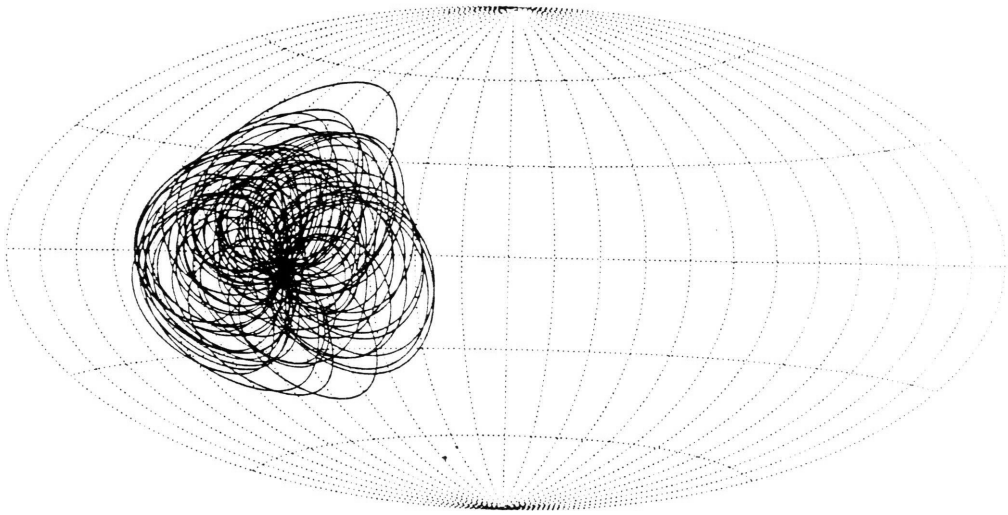

Figure 2.4. Illustration of event circles from a source, in this case a gamma ray burst (Winkler *et al.*, 1992). The most probable source location is near the point where the event circles intersect.

The characteristics of COMPTEL in performing gamma ray line spectroscopy are energy dependent. From pre-flight calibration measurements, the instrument's angular and energy resolution have been determined as a function of energy (Schönfelder *et al.*, 1993). The 1σ angular resolution (degrees), is given by

$$\sigma(E) = \frac{1.247}{1-e^{(-0.854\, E_{MeV}^{0.9396})}} \qquad (2.2)$$

and the 1σ energy resolution (MeV) is given by

$$\sigma_{MeV}(E) = 0.01 \sqrt{14.61\, E_{MeV} + 2.53\, E_{MeV}^2} \quad . \qquad ...(2.3)$$

For $E_{MeV} = 2.223$, the angular resolution is 1.5 degrees and the energy resolution is 67 keV (7.1% FWHM). Studies of 2.2 MeV line emission using in-flight COMPTEL data have shown the line width to be approximately 80 keV (Weidenspointer 1994, and

Rank, private communication), or 8.5% FWHM. This reason for this discrepancy is that the in-flight gain corrections (based on the ^{60}Co measurements) are not as effective in correcting for in-flight gain variations as they were during (ground-based) calibrations. Studies using in-flight data are therefore based on the larger line width.

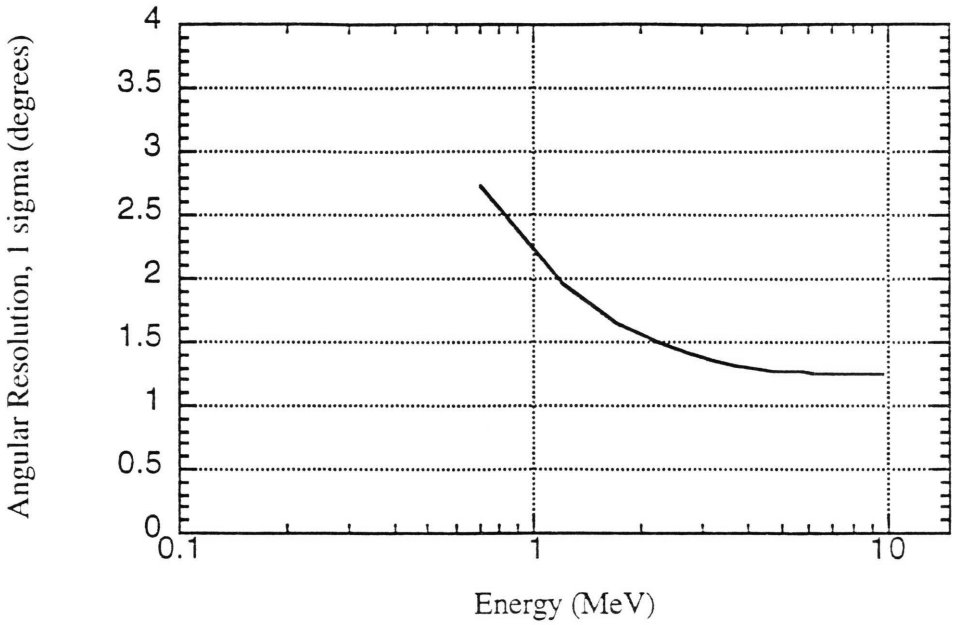

Figure 2.5. COMPTEL's angular resolution as a function of energy, determined from pre-flight calibration data.

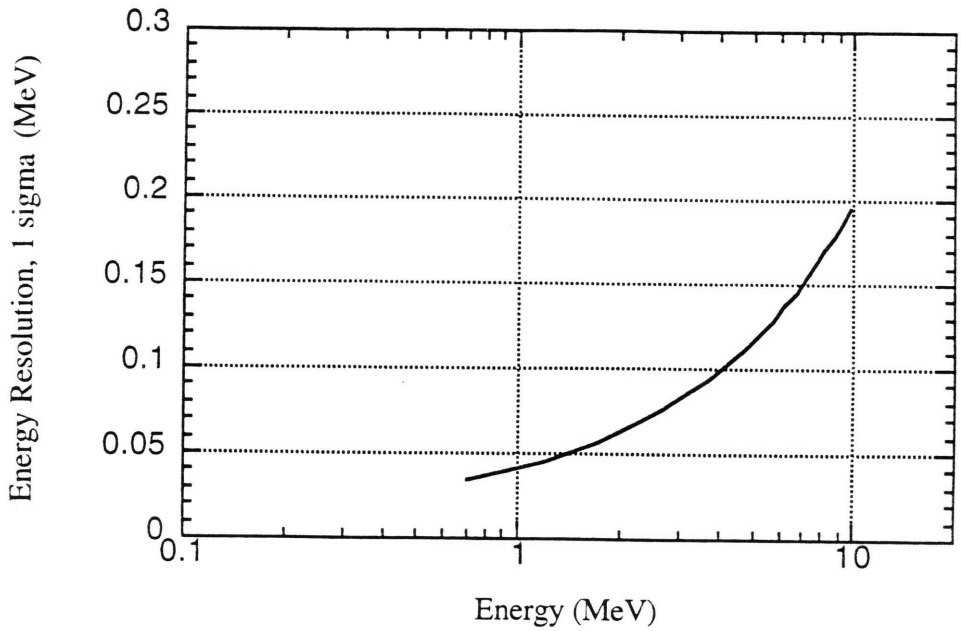

Figure 2.6. COMPTEL's energy resolution as a function of energy, determined from pre-flight calibration.

2.2.1 Rejecting Background Events With Data Cuts

Since COMPTEL is a background-dominated experiment with a small effective area, the rejection of background events is vital in obtaining a favorable sensitivity. Various types of background can be removed or mitigated by imposing various selection criteria on each event. As noted earlier, PSD and ToF selections can be used to reject neutron-induced events and to select only forward moving events, respectively. The Earth's atmosphere is also a source of gamma rays. In order to minimize the effect of this atmospheric background, it is useful to define an Earth Horizon angle (EHA) for each event. An event's EHA is defined to be the smallest angle between the (χ,ψ) scatter direction and the Earth's horizon. A second parameter (ζ) is then used to define the smallest angle between the event circle and the Earth's horizon (ζ = EHA-$\bar{\phi}$). By

specifying a suitable value for the minimum acceptable ζ (typically 5° or 10°), we can dramatically reduce the contribution of atmospheric gamma rays. Selections on D1E, D2E and $\bar{\phi}$ affect the field of view of the telescope. The D1 threshold defines the lower limit and the D2 threshold defines the upper limit of accepted scattered angle $\bar{\phi}$, as can be seen in Equation 2.1. For our study, we use the standard COMPTEL data selection criteria for the D1 and D2 thresholds. For the 2.2 MeV line, the D1 threshold gives a minimum acceptable scatter angle of 7° and the D2 threshold yields a maximum acceptable scatter angle of 64°. The $\bar{\phi}$ selection further restricts the telescope's field of view. The complete set of the selection criteria for this study is given in Table 2.2.

Table 2.2. Selections on COMPTEL data used in this study.

D1	70 - 20000 keV
D2	650 - 30000 keV
PSD	40 - 100 channels
ToF	115 - 130 channels
ζ	5 - 10 degrees
$\bar{\phi}$	0 - 36 degrees

These selection criteria reduce the background events considerably without removing many of the source gamma rays we wish to study. Even so, approximately 95% of the remaining events are background events (Knödelseder 1994). Other background components, which are difficult to reject, will be discussed further in the next section.

2.2.2 COMPTEL Background Spectrum

To illustrate what typical COMPTEL background data can look like, we selected a high-galactic latitude viewing period and generated an energy spectrum using the standard selection criteria outlined in Table 2.2. This spectrum is displayed in Figure 2.7. There are significant line features at 1.4 MeV and 2.2 MeV. The 1.46 MeV line results from ^{40}K

which is in the instrument itself (principally from glass in the D1 detector assemblies). The 2.2 MeV feature is also an internally generated line caused by ambient neutrons (principally from the Earth's atmosphere) being captured on the hydrogen in the low-Z D1 detector of COMPTEL. A detailed study of COMPTEL's instrumental 2.2 MeV line (and its dependence on various orbital parameters) was described by Weidenspointer (1994).

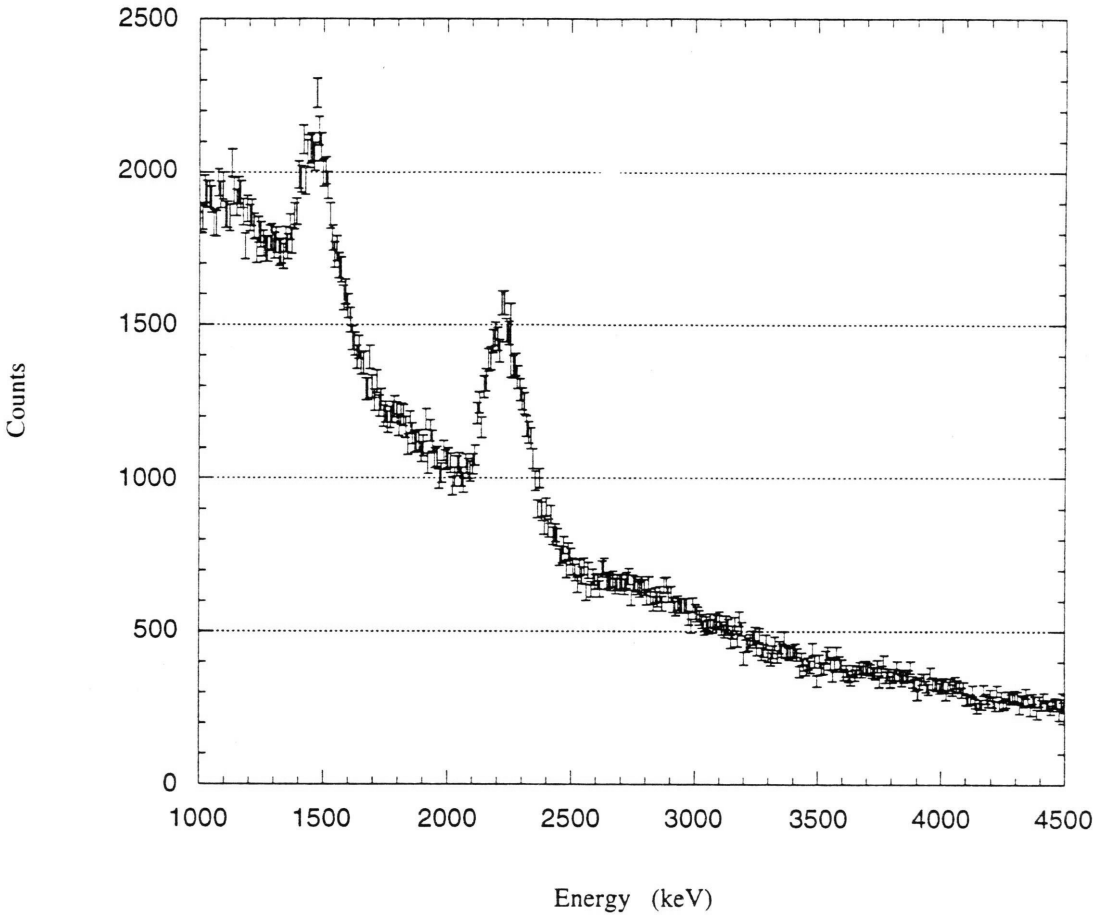

Figure 2.7. Energy spectrum from 1 to 5 MeV for a high-latitude observation. Note the features at 1.4 MeV and 2.2 MeV.

2.2.3 COMPTEL Line Sensitivity

To determine the line sensitivity (F_{lim}) of COMPTEL, we use the formula

$$F_{lim} = \frac{n\sqrt{S+B}}{A_{eff}\,T_{eff}} \tag{2.4}$$

where n is the number of sigma (in our case, we work with n = 3 or 3σ); S is the number of counts attributed to the source, which is set to zero to determine the line sensitivity; B is the number of counts assigned to the background; A_{eff} is the effective area of the detector and T_{eff} is the instrument live time. The two quantities, A_{eff} and T_{eff}, multiplied together give an effective exposure (cm^2 sec) for the instrument.

At 2.2 MeV, the photopeak effective area of the instrument is ~ 15 cm^2 (defined to be $\pm$ 1.41σ around the peak) (Schönfelder *et al.*, 1993). From Virgo region measurements, where no 2.2 MeV point sources are expected, we have measured the background counting rate in the photopeak energy interval. The background counting rate in this energy range will be enhanced because of the additional emission from the internal 2.2 MeV line. A measured counting rate of 0.03 counts/second gives the 3σ line sensitivity to be 5.5 x 10^{-5} $cm^{-2}s^{-1}$ for 2.2 MeV emission. This number represents a typical COMPTEL observation (two weeks duration). The total exposure over the first three phases of the mission leads to a more typical (total) line sensitivity of 2.5 x 10^{-5} $cm^{-2}s^{-1}$ for 2.2 MeV emission.

2.2.4 COMPTEL Dataspace and Instrument Response

The imaging analysis of COMPTEL data typically takes place in a three dimensional dataspace, defined by $(\chi,\psi,\bar{\phi})$. The angles (χ,ψ) represent the photon scatter direction as projected onto the sky. In this work, they represent Galactic longitude (l) and Galactic latitude (b), but they can refer to any co-ordinate system (e.g., celestial co-ordinates). The angle $\bar{\phi}$ represents the Compton scatter angle as derived from measured event parameters

(Equation 2.1). The dataspace binning used in this analysis for the (χ,ψ, $\bar{\phi}$) dataspace is 1° x 1° x 2°.

Crucial to any modeling procedure is the knowledge of how the instrument responds to a point source of radiation. The distribution of events in the 3-dimensional dataspace resulting from the presence of a single point source is known as the Point Spread Function, or PSF. The PSF can be determined by empirical measurements and/or simulations. We have used simulated PSFs in the present analysis (Stacy *et al.*, 1995). The PSF incorporates the errors inherent in the measurement of the event parameters. In the COMPTEL dataspace, the PSF is a cone centered at the source location (χ_0,ψ_0) with an opening angle of 45° (see Figure 2.8). The ideal events lie along the surface of the cone. Non-ideal events tend to fall inside the cone.

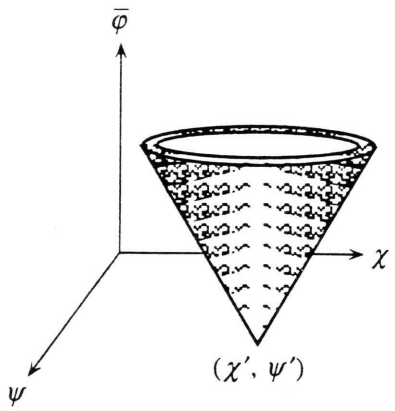

Figure 2.8. The cone of events from a point source located at (χ',ψ').

The COMPTEL instrument response to an arbitrary distribution of radiation is represented by the equation

$$n(\chi,\psi,\bar{\phi}) = g(\chi,\psi,\bar{\phi}) \int_{\chi_0,\psi_0} A(\chi_0,\psi_0)\, t\, I(\chi_0,\psi_0)\, f(\chi,\psi,\bar{\phi}|\chi_0,\psi_0)\, \partial\chi_0\, \partial\psi_0 \tag{2.5}$$

where $n(\chi,\psi,\bar{\phi})$ is the number of counts in the dataspace bin (χ,ψ,$\bar{\phi}$) and $g(\chi,\psi,\bar{\phi})$ represents the geometry of the two detector layers (essentially the probability that a photon

scattered in D1 will intersect the D2 layer). The effect of the various data selections comes in primarily through the geometry factor. The quantity $A(\chi_0,\psi_0)$ reflects the D1 effective area and t is the observation time. The quantity $I(\chi_0,\psi_0)$ is the intensity of the source. The Point Spread Function is represented by $f(\chi,\psi,\bar{\phi}|\chi_0,\psi_0)$. This complicated expression represents our theoretical dataspace, background with source, upon which our imaging procedures are based.

2.4 Data Analysis

This section discusses the methods used to analyze the data for our study of the celestial 2.2 MeV line. Two alternative approaches to generating images are first described. Then we discuss some of the different ways background models can be produced for COMPTEL dataspace. These background models are then compared with one another in the context of the 2.2 MeV line search.

2.4.1 Imaging Methods

There are two fundamental approaches to imaging the sky using COMPTEL data. These are the maximum entropy technique and the maximum likelihood technique, each of which are discussed in the following sections.

2.4.1.1 Maximum Entropy Deconvolution

The Maximum Entropy Method (MEM) is an iterative process which seeks to find the "flattest" distribution of emission which is consistent with the data. The use of this method for COMPTEL data analysis is discussed in Strong *et al* . (1991). In an effort to obtain a unique solution to the imaging problem, the maximum entropy method not only minimizes the standard χ^2 statistic, but it also seeks to maximize the configurational entropy, S. This quantity S is a measure of the number and complexity of structures in the map.

$$S = - \Sigma p_j \log (p_j/w_j) \qquad (2.6)$$

where $p_j = w_j f_j / \Sigma w\, f$, f_j is a skymap pixel and w_j is a weighting factor. The quantity S is summed over all skymap pixel j. In the application of this method to COMPTEL data, one starts out with a first estimate of the distribution of events in the 3 dimensional dataspace. This estimate is typically based on some background model (or models) plus some assumed source intensity distribution folded through the instrument response. For the initial starting point, a flat (i.e., featureless) point source distribution is assumed. The χ^2 criterion is checked for agreement between the real data and the trial skymap. For the maximum entropy method, the maximization of the entropy function is compared to the maximization of the original (flat) entropy function. Corrections to the assumed source intensity distribution are then made based on the results of this comparison and another iteration is performed. This iterative process is repeated until a suitable map is found.

In reality, determining which iteration of the maximum entropy method is the "correct" one is difficult. The choice of the most optimum iteration tends to be rather subjective, usually based on the appearance of the image. To determine which structures are real and worthy of further study, one must see which structures show up consistently over successive iterations. These features should not be considered real until they are investigated using a more rigorous (i.e., quantitative) method.

The maximum entropy method has been used to produce the all sky maps at 2.2 MeV (see Section 3.1) because it is much less CPU-intensive than the other method described in the next section. Potential sources, which appear as "hot spots" over several iterations, were subsequently examined in a more detailed, quantitative manner, using a maximum likelihood analysis (Section 2.4.1.2). Within the context of the COMPTEL Processing and Analysis Software (COMPASS), the maximum entropy method is implemented in the task SKYMEM.

2.4.1.2 Maximum Likelihood Deconvolution

As applied to COMPTEL data analysis, the Maximum Likelihood Method (MLM) is a more quantitative approach than that of maximum entropy. This method is better for determining flux values (or upper limits) at potential source sites. The application of the Maximum Likelihood Method to COMPTEL data analysis is discussed in de Boer *et al.*. (1991). Given any set of data, one can calculate the probability of obtaining those measurements. The probability of a given parameter θ is called its likelihood, $L(\theta)$. If there are two hypotheses, H_0 and H_1, the likelihood ratio of $L(H_0)/L(H_1)$ is a measure of how well the data support hypothesis 0 over hypothesis 1. Our likelihood function, which we want to maximize, looks like

$$L(\{n_i\}|H) = \prod e_i^{n_i} \exp(-e_i)/n_i!. \tag{2.6}$$

where i is bin number, n is number of counts, and e_i is the number of photons per time per unit bin times the integration time. To apply this to COMPTEL dataspace, we examine H_0 as the hypothesis that the data contains only background and H_1 as the hypothesis that the data contains both background and a single point source (as folded through the instrument response). Note that H_1 incorporates H_0. After each likelihood has been independently maximized, we look at the ratio of these likelihoods. We define a parameter

$$\lambda = -2 \ln \left[\frac{L(\{n_i\}|H_1)}{L(\{n_i\}|H_0)} \right] \tag{2.7}$$

where the quantity λ will follow the normal χ^2 distribution function for three degrees of freedom, where the three degrees of freedom are source position χ,ψ and intensity. This likelihood ratio of $L(H_0)/L(H_1)$ is determined at every point in the image. These values represent the relative probability of a model containing background plus a point source (at

that location) to a model containing only background. This method is also applicable if a field has more than one source. If the first process finds evidence for a source, then it is possible to add this source to the background hypothesis (which now becomes H_0) and the new H_1 is the new H_0 plus another source.

The use of the maximum likelihood method is computationally intensive so we restrict its application to small sections of the sky. The benefit of using this method is the ability to quantitatively test the probability of a source detection and to acquire flux estimates. Our results for the sky map hot spots (Section 3.1), the 20 target XRBs (Section 3.2) and the orbital phase-resolved analysis of Cygnus X-1 and Cygnus X-3 (Section 3.3) were generated using this method. The maximum likelihood method is implemented in the COMPASS environment as the task SRCLIK.

2.4.2 Background Model Generation

Both the Maximum Entropy Method and the Maximum Likelihood Method require a careful estimate (or model) of the instrumental background. The COMPTEL team has developed several methods to determine a background model for a given observation. One such model involves smoothing over the three dimensional dataspace. Other models are built up by defining two distributions - one for (χ,ψ) and one for $\bar{\phi}$. Taken together, these two distributions define the distribution of the background events in the full 3 dimensional dataspace. Here we shall review some of the background models relevant to the present study.

2.4.2.1. Smoothing Over The Dataspace

One of the more successful approaches to COMPTEL background modeling involves generating an estimate of the background by smoothing the measured dataspace. The smoothing eliminates (to first order) any source signatures which may be present in the

data. A region of 3^o x 3^o x 13^o is defined about each point in the $(\chi,\psi,\bar{\phi})$ dataspace (see Figure 2.9 a). The central 3^o x 3^o x 5^o area is excluded for the purposes of smoothing. Then the 3^o x 3^o bins in (χ,ψ) are averaged, reducing the statistical fluctuations inherent in the observation dataset. For the $\bar{\phi}$ distribution, a profile is fitted to the dataspace in the $\bar{\phi}$ direction. The profile is of the form

$$P(\chi,\psi,\bar{\phi}) = G(\chi,\psi,\bar{\phi})\frac{\Sigma_{\chi',\psi'} N(\chi',\psi',\bar{\phi}')}{\Sigma \quad G(\chi',\psi',\bar{\phi}')} \tag{2.8}$$

where the geometry matrix $G(\chi,\psi,\bar{\phi})$ is normalized to the number of observed photons for a given $\bar{\phi}$, hence the sum over (χ',ψ'). The actual background model is this profile than normalized over the $\bar{\phi}$ range used in the fitting (hence the sum over $\Delta\bar{\phi}$) which looks like

$$B(\chi,\psi,\bar{\phi}) = P(\chi,\psi,\bar{\phi})\frac{\Sigma_{\Delta\bar{\phi}} \langle N(\chi',\psi',\bar{\phi}') \rangle}{\Sigma_{\Delta\bar{\phi}} P(\chi',\psi',\bar{\phi}')} \; . \tag{2.9}$$

In practice, the use of this smoothing technique also requires modifications to the PSF (Figure 2.9.b) (Bloemen *et al.*, 1993). The COMPASS program BGDLIX generates this background model as an independent dataset, which can be used in various imaging programs (although without the PSF modifications). It is also the default background method when using the maximum likelihood method program SRCLIX, which does incorporate the necessary PSF modifications. As such, SRCLIX is the preferred tool for implementing this approach.

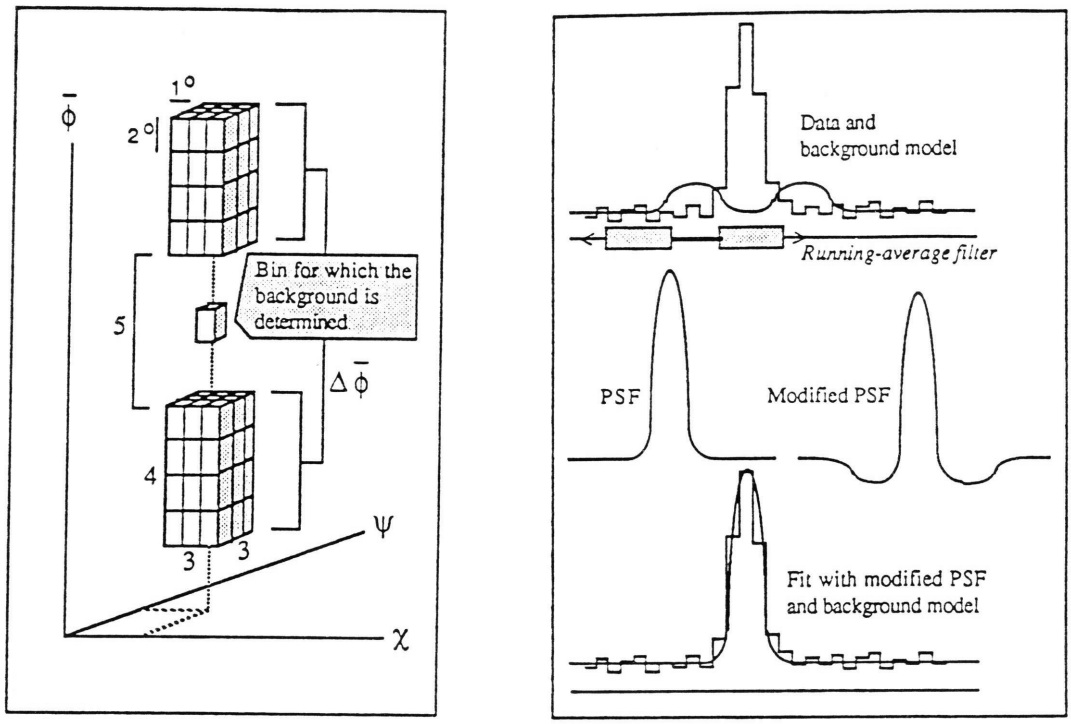

Figure 2.9. a) The data bins used for smoothing in the default background generation and **b)** the PSF modification performed in the program SRCLIX [from Bloemen *et al.*, 1993].

2.4.2.2 Background Modeling at 2.2 MeV

As a first step towards developing a background model specifically designed for the 2.2 MeV line, we attempted to model the $\bar{\phi}$ spectrum in a narrow energy range centered on 2.2 MeV. This initial effort was motivated by the knowledge (based on simulations) that the $\bar{\phi}$ spectrum of the internal 2.2 MeV line provided a very unique signature. In particular, the $\bar{\phi}$ spectrum of the internal 2.2 MeV background has a much greater contribution at higher $\bar{\phi}$ values than does the $\bar{\phi}$ spectrum of an external point source (see Figures 2-10a and b). By exploiting this difference in the energy spectra at higher $\bar{\phi}$ values, we hoped to obtain the contribution of the internal 2.2 MeV line to the background, which would then allow us to assemble a background model.

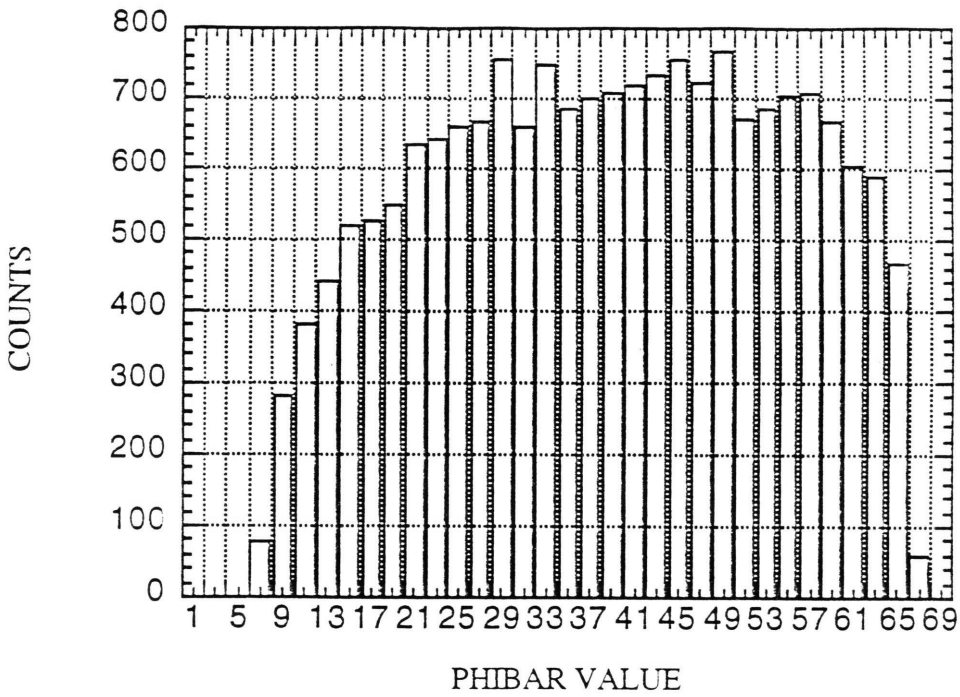

Figure 2.10. a) The $\bar{\phi}$ spectrum for an internal (diffuse) source of 2.2 MeV photons.

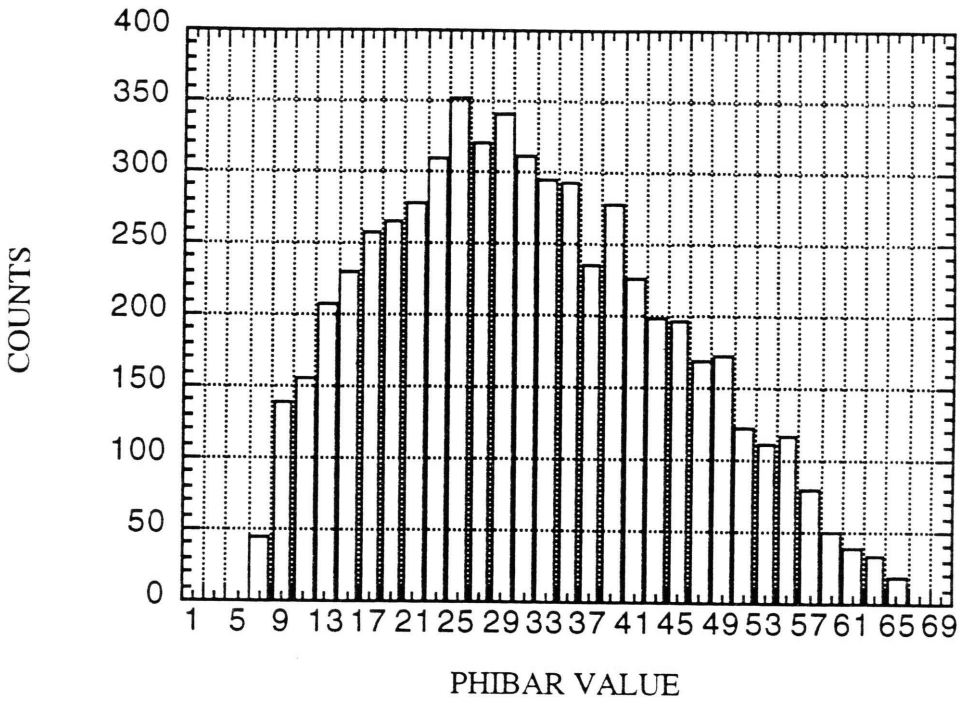

Figure 2.10 b) The $\bar{\phi}$ spectrum for an external point source of 2.2 MeV photons.

Our attempt to model the real data $\bar{\phi}$ spectrum from the 2.2 MeV line energy interval was based on a linear combination of two independent $\bar{\phi}$ spectra: one taken from the simulations of the internal 2.2 MeV background and one taken from the real data in an energy band just above the 2.2 MeV line. Here we made the critical assumption that the $\bar{\phi}$ spectrum from the real line energy interval would be the same as the slightly higher energy interval if there were no internal 2.2 MeV line. We had two independent checks on this fitting procedure. In the first check, the 3 dimensional datasets for the simulated 2.2 MeV line and the adjacent high energy interval were used as background models in maximum likelihood imaging of runs for the 2.2 MeV line energy interval. This provided an estimate of the internal 2.2 MeV line emission, based on the fitted contribution of the 2.2

MeV component of the background model.. In the second check, the total energy spectrum (E1 + E2) was fit with a continuum background and a Gaussian centered at 2.2 MeV, giving a second estimate of the internal 2.2 MeV line contribution (assuming no external sources were present). Ideally, both approaches should have given consistent results. Unfortunately, we were not able to develop a self-consistent model using this approach.

There are at least two possible reasons for the difficulties we encountered with this method. One is that the 'high' energy interval may have been insufficient to model that part of the line interval data not associated with the 2.2 MeV background. Perhaps a combination of 'lower' and 'higher' energy intervals should be combined to model the $\bar{\phi}$ spectrum for the line interval data. However, we wanted to avoid using the lower energy interval, because this $\bar{\phi}$ spectrum might be contaminated with incompletely absorbed internal 2.2 MeV line emission. A second possible explanation for the modeling difficulties stems from the existence of ^{24}Na cascade lines in the COMPTEL background. Cascade lines are created when an excited nucleus decays, producing two photons simultaneously. In the case of ^{24}Na, the two emitted photons have energies of 1.37 MeV and 2.75 MeV. These cascade lines add a wide "bump" in the COMPTEL energy spectrum at a few MeV (Knödelseder 1994). Perhaps simulated cascade lines should be included in the background model for a more accurate representation of the line energy dataspace. Clearly, more work could be done to develop such a 2.2 MeV background model. In order to make further progress in our study of the celestial 2.2 MeV emission, however, it was decided to apply another empirical background modeling procedure to our data.

2.4.2.3 Background Modeling for Gamma Ray Line Studies

This approach uses the $\bar{\phi}$ distribution from the 2.2 MeV line interval as the $\bar{\phi}$ distribution of the background dataset. In order to estimate the (χ,ψ) distribution, we note that this distribution has been found to be independent of energy (Knödelseder 1994). We therefore use the energy range 1-10 MeV to determine the (χ,ψ) distribution of the

background dataset. The resulting three dimensional (χ,ψ,$\bar{\phi}$) distribution is smoothed via convolution with a Gaussian, with greater smoothing at higher $\bar{\phi}$ where the number of counts is much lower. Finally, the background is normalized to a "narrow" energy interval, defined to be centered on the line but twice the energy width of the line. The line energy interval counts are subtracted from the narrow line energy interval. The remaining counts are then used to normalize the background model. This background generation procedure was developed in conjunction with the 1.8 MeV studies of the Galactic plane (Diehl 1995). The background model is generated by the COMPASS task BGDLNE.

The line energy interval is selected to maximize the signal-to-noise ratio of the 2.2 MeV line. If we assume that we have much greater background than signal ($N_B >> N_S$), the signal-to noise ratio can be expressed as

$$\frac{\text{Signal}}{\text{Noise}} = \sqrt{\frac{N_S}{N_B}} \quad . \tag{2.10}$$

If we further assume a Gaussian line shape for the signal (N_S) and that the background (N_B) is flat , we can then maximize this ratio with the respect to an energy interval, finding that the signal-to noise ratio is greatest when the energy interval is 1.2 times the FWHM. Since COMPTEL's energy resolution at 2.2 MeV has been experimentally shown to be approximately 80 keV, our optimal line energy interval is calculated to be 2.11-2.34 MeV.

2.5 Testing of Background Model

In order to confirm the efficiency of the BGDLNE background model, three types of imaging tests were performed. The first test was a null test, imaging a region of the sky where we expected no 2.2 MeV sources. The second test was an image of a strong continuum source with no line emission present. This was performed in order to ensure proper handling of the source continuum component. Finally, a solar flare with a strong

2.2 MeV line was imaged. This would show how well a positive 2.2 MeV signal would be handled. The first two tests were performed separately for each phase (1, 2, and 3) and then for the sum of all three phases (1-3). All viewing periods were used with the exception of two. Viewing period 2.5 was rejected because COMPTEL was operating in a different mode (to detect solar neutrons). The combined viewing periods (41+44) were also not used, pending an updated processing of these datasets. The positive test of the solar flare was performed only once to ensure that the analysis of a known source of 2.2 MeV emission, already studied in detail by Rank (1995 - to be published), would give a correct result.

2.5.1 The Null Test

For the null test, we chose a high-latitude observation which is expected to be relatively free of both the diffuse galactic emission and intense point sources. Although the Virgo region has a few variable emitters in the low MeV range (e.g., 3C 273 and 3C 279), there are no X-ray binary candidates which might be considered as potential sources of 2.2 MeV line emission. Our imaging tests concentrated on a part of the field which contained no known or suspected sources of 2.2 MeV emission.

Table 2.3. The maximum likelihood ratios and significance for the Virgo region test.

OBSERVATION	λ	n_σ
Phase 1	2.0	0.6
Phase 2	7.2	1.8
Phase 3	5.1	1.4
Phases 1-3	2.7	0.8

The results from each of the four Virgo region maps are all under 2σ (for 3 degrees of freedom) (see Table 2.3). The four MLM maps of the Virgo region are shown in Figures 2.11 - 2.14. This demonstrates that for a field which is expected to contain no sources of 2.2 MeV emission, the resulting image is free from appreciable artifacts. In other words, we generate no false positive detections.

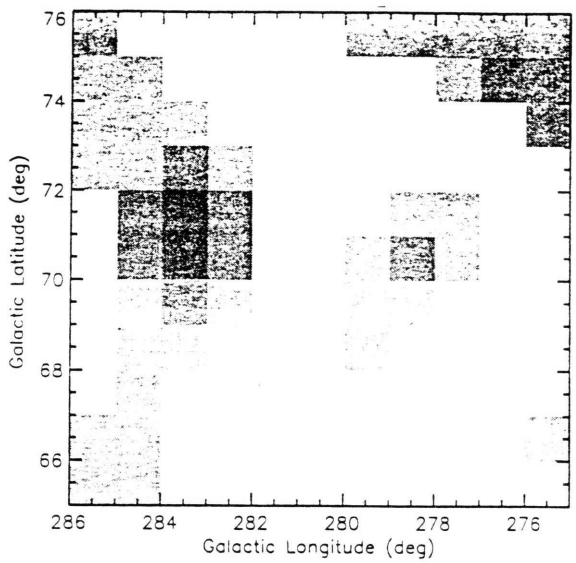

Figure 2.11 Phase 1 Virgo Region maximum likelihood map generated with line background model.

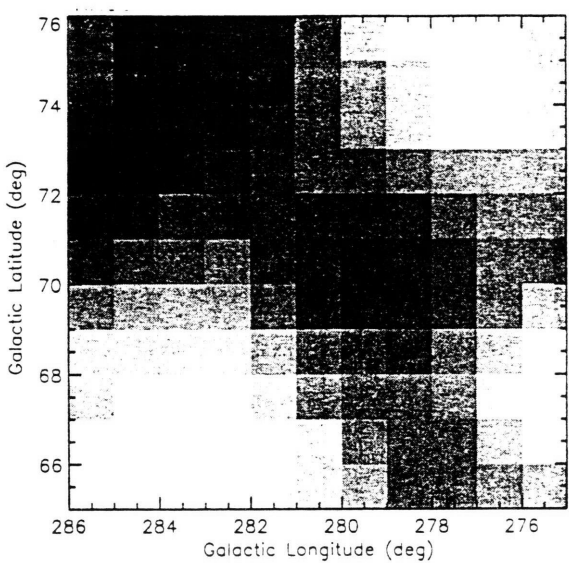

Figure 2.12 Phase 2 Virgo Region maximum likelihood map generated with line background model.

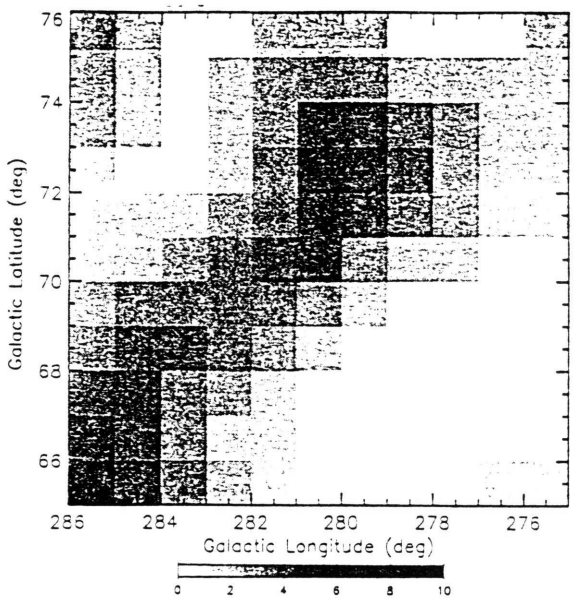

Figure 2.13 Phase 3 Virgo Region maximum likelihood map generated with line background model.

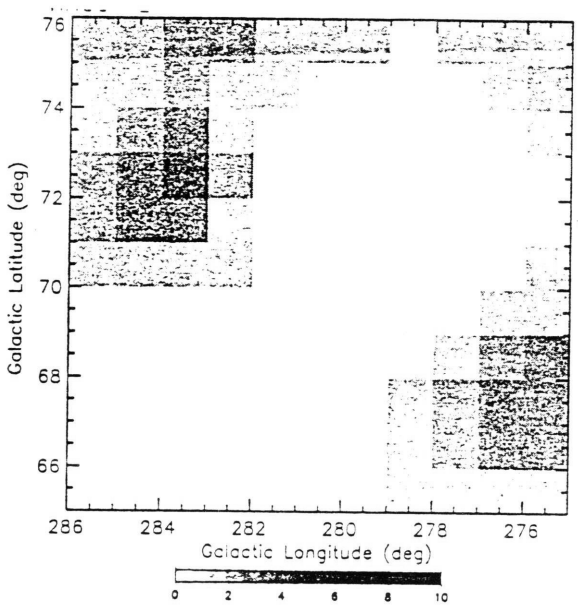

Figure 2.14 Phases 1-3 Virgo Region maximum likelihood map generated with line background model.

2.5.2 The Continuum Source Test

Since the line background modeling procedure was designed to eliminate all continuum sources, the strongest gamma ray continuum source in the 1-3 MeV range was used to test the model - the Crab nebula/pulsar. There are also no known mechanisms for the Crab pulsar to emit a line at 2.2 MeV, making it an excellent test object. Because the location of the Crab pulsar is known, only 1 dof exists (intensity), and $\lambda = 9$ represents a 3σ detection. For comparative purposes, the background model generated by smoothing the dataspace (Section 2.2.4.1.) was used on the same datasets.

Table 2.4. Maximum likelihood ratios at the Crab pulsar location, l =184.6, b =-5.8.

Observation	Smoothed Background		Line Background	
	λ	n_σ	λ	n_σ
Phase 1	70.1	8.2	6.13	2.5
Phase 2	25.6	5.0	0.76	0.9
Phase 3	69.8	8.1	4.93	2.2
Phases 1-3	160.0	12.3	2.00	1.4

There is considerable reduction of the Crab signal in each of the four tests and, in all cases, the resulting likelihood ratio is below a significance of 3σ. The four maximum likelihood maps of the region surrounding the Crab pulsar are shown in Figures 2.15 - 2.18. The measured likelihood ratios at the Crab location are listed in Table 2.4. Note that the likelihood ratio is always given as a positive quantity, even in those cases where the physical quantity of interest (e.g., counts attributable to a point source at that location) may actually be negative. This is exemplified here if we look at the derived source counts at the Crab location, as listed in Table 2.5. Note that the number of source counts (and, hence, the derived flux values given in Table 2.6) are negative in most cases. There is some residual emission at a level greater than 3σ in the maps for phase 1 and phases 1-3. This residual signal is, however, located away from the Crab's location. Furthermore, the number of counts derived at the location of the maximum excess (based in the summed data from phases 1-3) are all negative, suggesting an unphysical effect. These data tend to

suggest that some further refinement of the model may be possible, but that, to at least first order, the model is quite adequate.

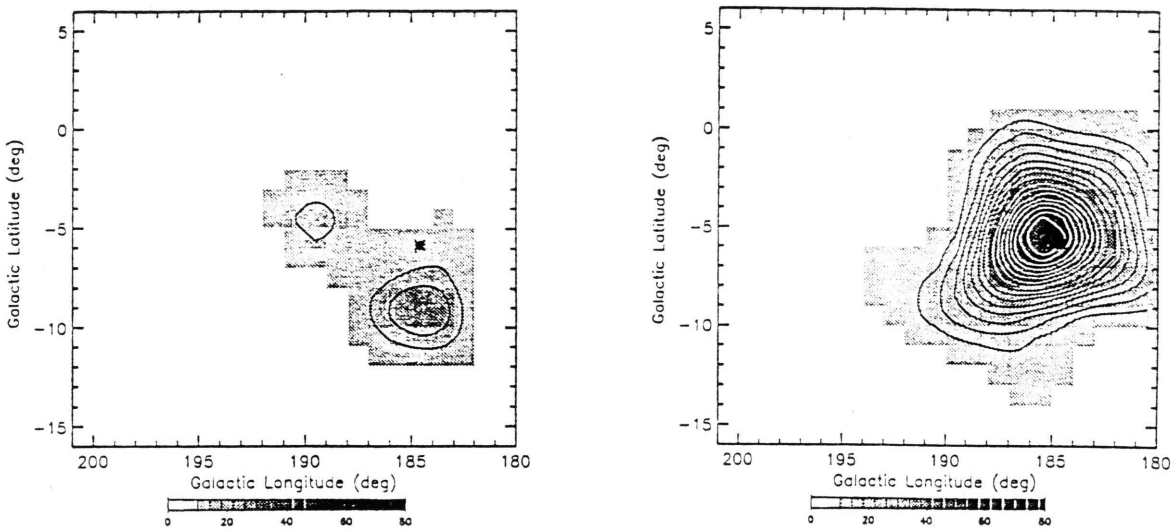

Figure 2.15. Phase 1 Crab region maximum likelihood map generated with smoothed background model (right) and line background model (left).

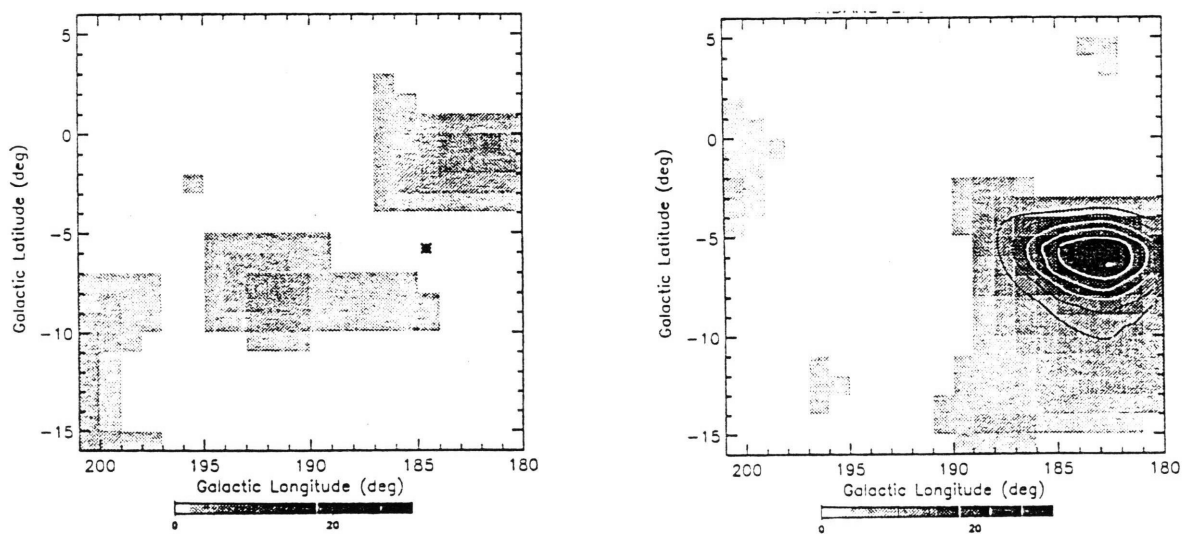

Figure 2.16. Phase 2 Crab region maximum likelihood map generated with smoothed background model (right) and line background model (left).

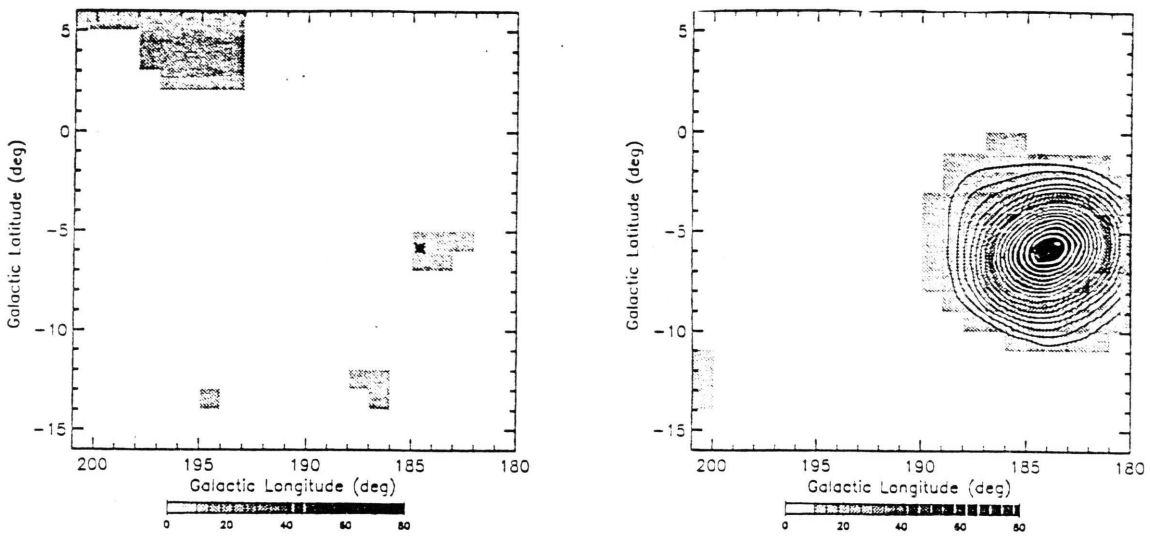

Figure 2.17. Phase 3 Crab region maximum likelihood map generated with smoothed background model (right) and line background model (left).

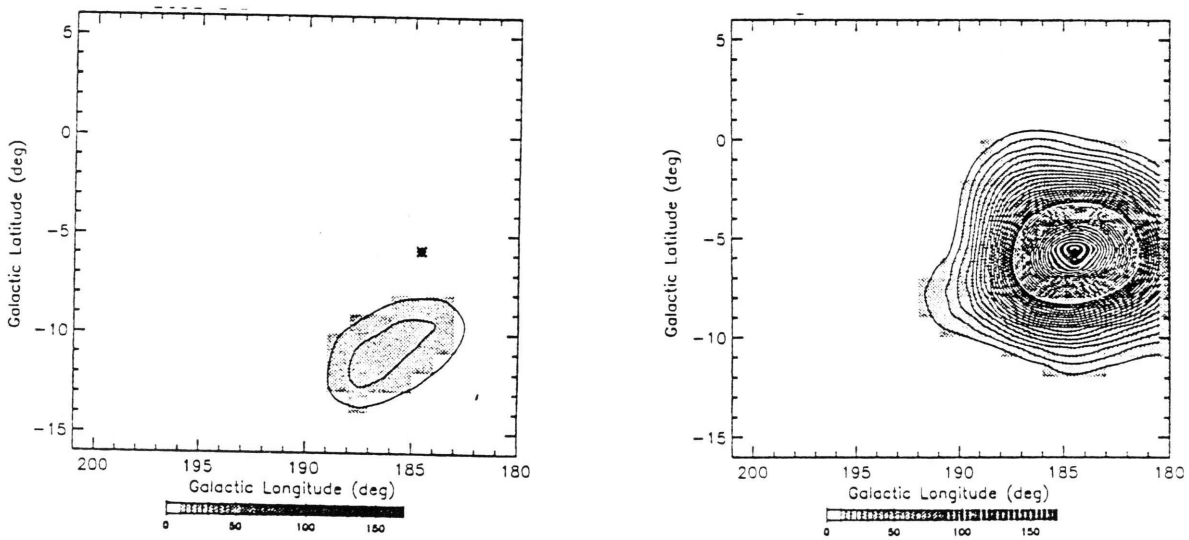

Figure 2.18. Phases 1-3 Crab region maximum likelihood map generated with smoothed background model (right) and line background model (left).

Table 2.5. Number of counts in the 2.11-2.34 MeV interval at the Crab position.

Observation	Smoothed Background	Line Background
Phase 1	1179 ± 145	-357 ± 144
Phase 2	360 ± 73	-55 ± 64
Phase 3	1067 ± 131	289 ± 132
Phases 1-3	2544 ± 206	-269 ± 205

Table 2.6. The 3σ upper limits on the Crab pulsar emission at the source location using the BGDLNE-generated background.

OBSERVATION	LINE FLUX	3σ UPPER LIMIT
	[x 10^{-5} photons / cm^2 s]	
Phase 1	-2.68 ± 1.08	3.24
Phase 2	-2.00 ± 2.32	6.95
Phase 3	2.86 ± 1.30	6.76
Phases 1-3	-1.13 ± 0.79	2.35

Table 2.7. The number of counts in the Crab region at the residual emission location from the phases 1-3 maximum likelihood map.

OBSERVATION	BGDLIX	BGDLNE
Phase 1	422 ± 137	-337 ± 137
Phase 2	235 ± 70	-64 ± 58
Phase 3	50 ± 127	-192 ± 127
Phases 1-3	580 ± 197	-775 ± 196

Notice that the counts from all four of the maximum likelihood maps which use the BGDLNE-generated background models are consistent with zero within 3σ. This is a valuable test on the data which shows that, while we obtain a greater than 3σ detection in the Crab region, the number of counts within the map are consistent with zero. This may be a reflection of the degree of difficulty to model the Crab pulsar emission. It may be impossible, or even unreasonable, to completely eliminate the Crab emission from the COMPTEL dataspace. This difficult may be due to the linear interpolation which occurs when the energy intervals which surround the line interval are used to normalize the model. This linear interpolation is slightly off from the Crab's spectral shape and this imperfect match may cause the residual emission (Oberlach, private communication). The fact that the number of counts in the Crab region maximum likelihood map are consistent with zero means that the "object" with a greater than 3σ detection would not be considered a source.

Using that criteria, we are able to say that this approach to modeling the background for gamma ray studies can effectively handle any continuum sources.

2.5.3 The 2.2 MeV Source Test

The 2.2 MeV neutron capture line is well documented as a major component of solar flare spectra (Section 1.2.1). Since COMPTEL has detected 2.2 MeV line emission from many solar flares, it was decided to select one as our test case for determining how well the background model works with a known 2.2 MeV line source. The June 11, 1991 solar flare was selected as the positive signal test. One advantage of studying a solar flare is the ability to generate an independent estimate of the background and to measure the total source counts using background subtraction on the solar flare's energy spectrum.

This background subtraction was performed in energy space, so we were generating spectra in total energy space (for example, the energy spectrum as shown in Figure 2.7). Approximately every 15 orbits, COMPTEL returns to the same geographic location with essentially the same geomagnetic conditions. This provides us with a background model, using real data, which is as close as possible to the background at the time of the event being studied. Typically we take two orbits, 15 orbits before and 15 orbits after the event, and average these to generate a background model in energy space. In the case of the June 11, 1991 flare, the orbit 15 after was unusable, so we used the 30th orbit after. The orbital background model is then subtracted from the solar flare energy spectrum. The remaining energy spectrum is due to the flare itself. This background subtracted energy spectrum is fit from 1.5 MeV to 3.0 MeV with a quadratic for continuum and a Gaussian for the line.

The results in Table 2.8 for all three methods show a very high detection significance and all of the measured line counts are consistent within 1-2σ. The maximum likelihood maps also indicate the strength of the source using both types of background models (see Figures 2.19 amd 2.20). This test of the background model on a known 2.2

MeV line source gives us confidence that 2.2 MeV line emission would be detectable using a BGDLNE-generated background model.

TABLE 2.8. Results comparing three background models using the June 11, 1991 flare.

		Smoothed Background	Line Background	Energy Spectrum
Solar Flare	λ =	368.9	334.5	
	counts =	407 ± 11	389 ± 29	270 ± 69

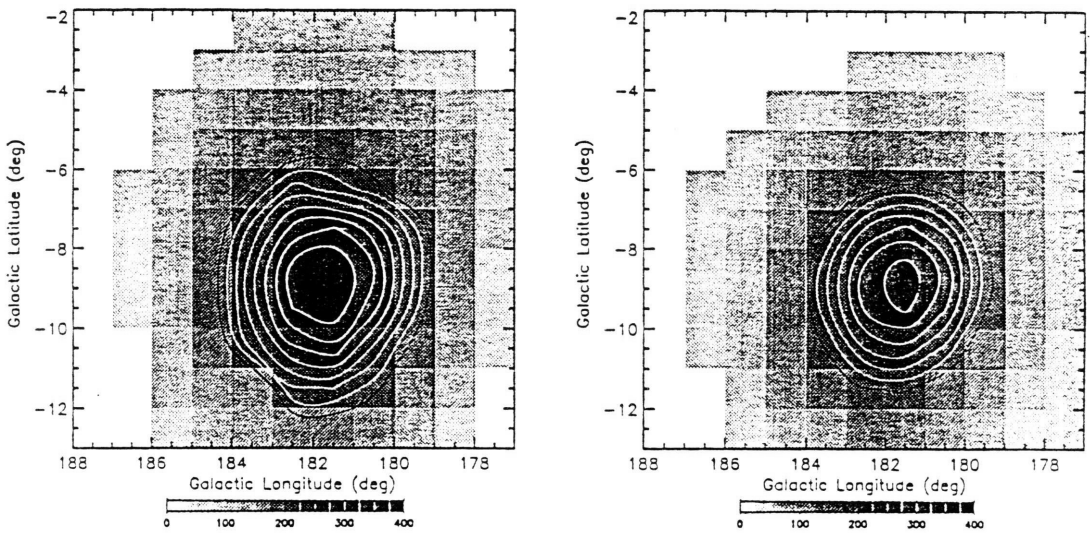

Figure 2.19. The June 11, 1991 solar flare maximum likelihood map generated using the dataspace smoothing background model (right) and the line background model (left).

We have shown that the background model generated by the COMPASS task BGDLNE is suitable for the purposes of studying 2.2 MeV line emission. It does not create artifacts in the data (the Virgo region test), it can adequately handle continuum emission (the Crab region test) and it does yield a reasonable result for a known positive source of 2.2 MeV line emission (the solar flare test). With these checks on the background model completed satisfactorily, we can then apply the background modeling procedure to the data we wish to study.

CHAPTER III
RESULTS

3.1 All Sky Maps

The COMPTEL data have been used to generate the first-ever all-sky maps at 2.2 MeV. These maps were generated using the maximum entropy technique. This technique was chosen for all-sky imaging because it is far less CPU-intensive than the corresponding maximum likelihood analysis. Background models were generated in the manner described in Section 2.4.2 for each viewing period separately, then summed as needed.

As discussed previously, it is difficult to decide which maximum entropy iteration represents the true source intensity distribution. We can only examine a series of iterations and select a map which looks "reasonable". Determining which features are real and which are artifacts is done by seeing which features" are stable from iteration to iteration and which ones appear and disappear randomly. These maximum entropy sky maps indicate regions which can be targeted for more quantitative study by another method. In this case, the potential hot spots were quantitatively analyzed using the maximum likelihood method. Maximum likelihood maps were generated for a small region around each identified hot spot. A source would be considered to as a possible detection if it had a likelihood ratio greater than 14.2 (which indicates a significance of 3σ or greater for three degrees of freedom).

Only one hot spot showed a significant likelihood value in the phase 1 data. It was located at (l,b) = (230.5, -43.5) and had a likelihood ratio of 19.1.

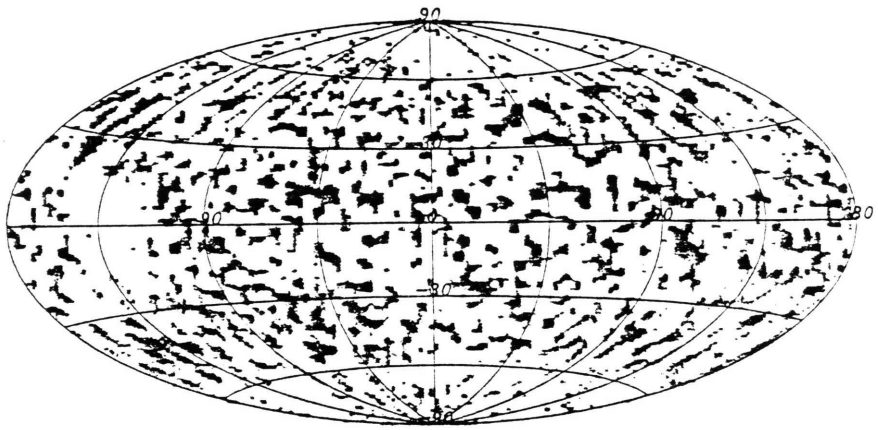

Figure 3.1. Phase 1 all sky map at 2.2 MeV.

In the phase 2 dataset, two features had a likelihood ratio greater than 14.2. They are located at $(l,b) = (55.1, -2.8)$ with $\lambda = 23.4$ and at $(l,b) = (262.3, 44.9)$ with $\lambda = 14.8$.

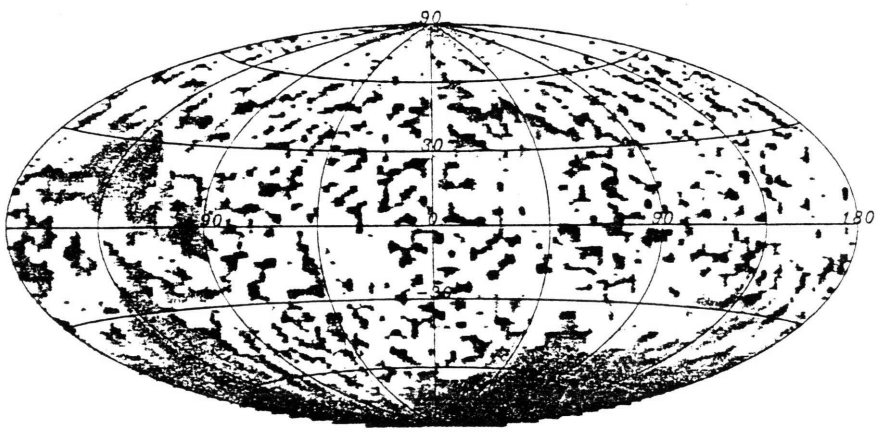

Figure 3.2. Phase 2 all sky map at 2.2 MeV.

None of the tested features in the phase 3 dataset had a likelihood ratio greater than 14.2.

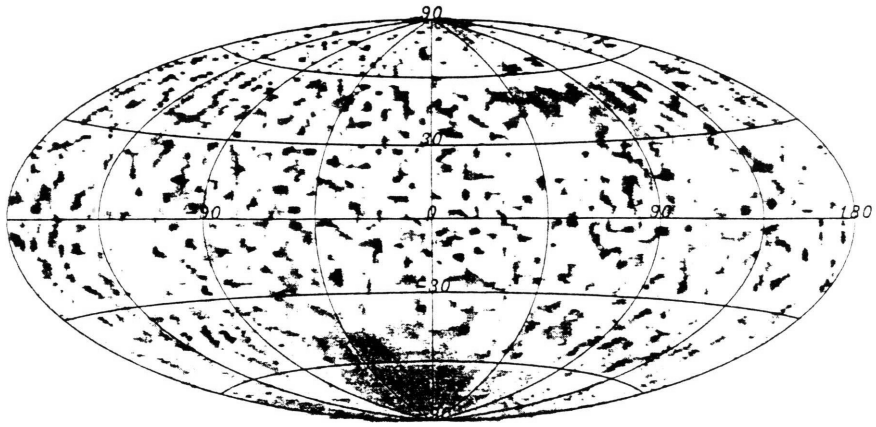

Figure 3.3. Phase 3 all sky map at 2.2 MeV.

When examining the combined phases 1-3 dataset, only one feature had a likelihood ratio greater than 14.2. This was located at $(l,b) = (54.5, -1.3)$ with $\lambda = 14.3$.

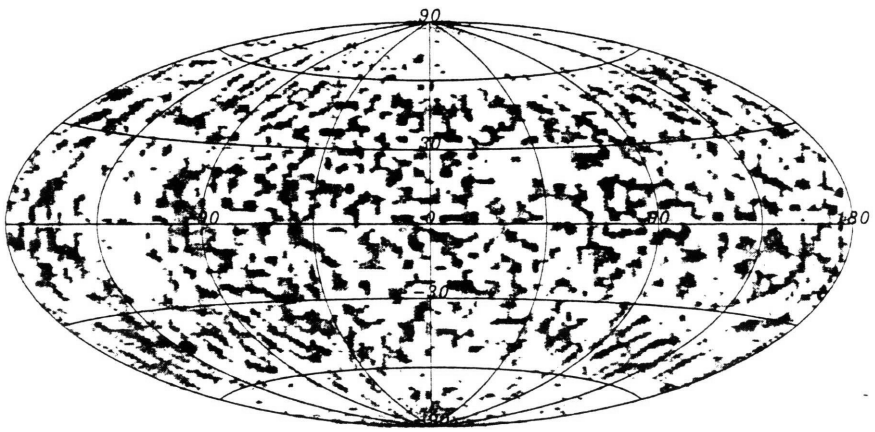

Figure 3.4. Phases 1-3 all sky map at 2.2 MeV.

Only two 'hot spots' could be considered as potential candidates for 2.2 MeV line emission: those near *(l,b)* = (55.1, -2.8) and *(l,b)* = (230.3, -43.5). The other two objects, *(l,b)* = (262.3, 44.9) and *(l,b)* = (54.5, -1.3), had likelihood ratios on the order of 14.2. These would be considered marginal detections. Note that the detection at (l,b) = (54.5, -1.3) in the phases 1-3 map is roughly consistent with that at (l,b) = (55.1, -2.8) found in the Phase 2 map. This source location area was checked in the other two phase datasets (1 and 3) but did not have a significance greater than 3σ.

Note that the significance levels which we ultimately quote for these features should incorporate the statistical effects which result from the number of effective trials. In this case, the number of trials is difficult to ascertain, due to the qualitative nature of the maximum entropy maps used to pick out the interesting features. In any case, the number of trials tends to reduce the significance of a given measurement. If, for example, we assume the number of trials to be 100 (not an unreasonable number considering that we have searched the entire sky), then the most significant of the above features (that which shows a likelihood ratio of 23.4) has a significance of just under 3σ. This would suggest that none of the effects noted above are significant.

3.2 Flux Values and Upper Limits for Target List

The data for this study was the same as used in the maximum entropy method all-sky map production. In this case, we generated maximum likelihood maps of small regions around each candidate source (see Section 2.4.1.2) using the gamma ray line background method (see Section 2.4.2.3). We are statistically able to claim a possible source detection if we obtain an appropriate likelihood value ($\lambda > 9.0$ for a known source, $\lambda > 14.2$ for a source search) which indicates 3σ or greater. (Again, we must ultimately incorporate the number of trials into our final significance levels for any positive detection.) In the case of a positive detection, we report a value for the line flux. If we have no detection (i.e., one less than 3σ significance), we report an upper limit for the flux.

We generate the upper limits in two different cases. The general equation for an upper limit

$$F \leq F_{lim} = F_o + n*\frac{\Delta c}{c}*F_m \qquad (3.1)$$

where F_m is the measured flux, Δc is the 1σ error in the number of measured counts, c is the number of counts, and n is the number of σ desired. We calculate 3σ upper limits to compare with the literature, so n = 3. The value of F_o depends on the measured flux. If the measured flux is zero or negative, one sets F_o equal to zero. This reflects no source detection and yields an indication of the sensitivity of COMPTEL. If the measured flux is greater than zero but does not have a significant detection (greater than 3σ), then one sets F_o equal to F_m. A positive flux cannot be ruled out, even though the detection is not significant enough, hence the upper limit must include the possibility that there is some source emission.

The following four tables (Tables 3.1 - 3.4) list the results for the 20 X-ray binaries selected for the maximum likelihood 2.2 MeV line flux study, one for each phase and the combined phases 1-3 data. To put the upper limits in proper context, the actual line fluxes and the 1σ error on these measurements are also included. The effective exposure listed in the tables represents the effective on-axis exposure (measured in days). This incorporates the effects of the off-axis angle of the source as well as Earth-occultation times and telemetry contact times.

Table 3.1. Line fluxes and 3σ upper limits for selected XRBs from Phase 1 data.

OBJECT (x 10^{-5} photons/cm^2 s)	LINE FLUX	3σ U. L. (days)	EFF. EXP.
Cyg X-1	-0.17 ± 1.24	3.71	10.11
Cyg X-3	0.22 ± 1.27	4.04	8.48
2000 + 251	1.30 ± 1.66	4.78	10.52
2023 + 338	0.45 ± 1.22	4.12	9.40
LMC X-1	-0.95 ± 0.93	2.78	13.19
LMC X-3	-1.38 ± 0.88	2.63	12.58
CAL 83	-0.81 ± 0.89	2.67	13.19
GX 339-4	-0.39 ± 1.35	4.06	10.05
SS 433	-1.47 ± 1.04	3.13	12.85
Aql X-1	-0.97 ± 1.03	3.09	12.78
Cen X-3	-1.31 ± 1.11	3.32	10.97
N Mus 91	-1.38 ± 1.11	3.32	11.29
Her X-1	2.11 ± 1.31	6.05	5.05
0115 + 63	1.44 ± 1.29	5.30	5.86
Vela X-1	-2.47 ± 1.17	3.51	10.34
CAL 87	-3.12 ± 1.04	3.13	11.30
Sco X-1	-1.96 ± 1.56	4.67	9.88
0620 + 00	2.15 ± 1.62	4.87	9.94
1755 - 338	-1.94 ± 1.62	4.87	12.25
Cir X-1	-1.13 ± 1.34	4.02	8.73

Table 3.2. Line fluxes and 3σ upper limits for selected XRBs from Phase 2 data.

OBJECT (x 10^{-5} photons cm^{-2} s^{-1})	LINE FLUX	3σ U. L. (days)	EFF. EXP.
Cyg X-1	3.17 ± 1.13	5.57	8.51
Cyg X-3	0.85 ± 1.08	4.09	8.77
2000 + 251	1.42 ± 1.25	5.16	6.12
2023 + 338	4.58 ± 1.16	*	7.85
LMC X-1	-1.76 ± 1.71	5.14	2.20
LMC X-3	-2.27 ± 1.84	5.52	1.99
CAL 83	-2.19 ± 1.74	5.51	2.15
GX 339-4	-2.18 ± 1.31	3.94	7.80
SS 433	0.14 ± 1.66	5.12	2.69
Aql X-1	0.73 ± 1.66	5.72	1.70
Cen X-3	0.72 ± 1.71	5.86	4.28
N Mus 91	-1.36 ± 1.83	5.48	3.11
Her X-1	-0.79 ± 1.42	4.25	3.13
0115 + 63	2.37 ± 1.40	6.58	3.13
Vela X-1	4.11 ± 2.62	11.99	1.06
CAL 87	0.67 ± 1.88	6.31	2.48
Sco X-1	-1.30 ± 1.69	5.06	5.30
0620 + 00	1.36 ± 2.96	10.25	1.83
1755 - 338	-0.98 ± 1.52	4.56	9.58
Cir X-1	-4.65 ± 1.34	4.02	6.86

* denotes a > 3σ flux value

Table 3.3. Line fluxes and 3σ upper limits for selected XRBs from phase 3 data.

OBJECT	LINE FLUX	3σ U. L.	EFF. EXP.
(x 10^{-5} photons/cm^2 s^1)		(days)	
Cyg X-1	0.49 ± 1.30	4.39	9.57
Cyg X-3	1.83 ± 1.35	5.88	8.66
2000 + 251	1.49 ± 1.29	5.36	9.38
2023 + 338	-0.81 ± 1.30	3.90	9.30
LMC X-1	-3.36 ± 1.33	3.98	6.26
LMC X-3	-3.68 ± 1.21	3.63	5.70
CAL 83	-3.94 ± 1.29	3.86	6.40
GX 339-4	-0.76 ± 1.38	4.13	11.04
SS 433	-2.68 ± 1.18	3.55	10.31
Aql X-1	-1.56 ± 1.16	3.48	12.11
Cen X-3	1.13 ± 1.27	4.96	8.36
N Mus 91	0.36 ± 1.33	4.34	7.85
Her X-1	-2.00 ± 2.32	6.95	2.04
0115 + 63	0.04 ± 1.57	4.75	4.06
Vela X-1	2.97 ± 1.16	6.45	5.98
CAL 87	-1.13 ± 1.21	3.63	8.20
Sco X-1	-0.55 ± 1.75	5.25	12.28
0620 + 00	0.77 ± 1.30	4.67	8.44
1755 - 338	-0.58 ± 1.62	4.87	14.36
Cir X-1	0.52 ± 1.38	4.65	7.78

Table 3.4. Line fluxes and 3σ upper limits for selected XRBs from phases 1-3 data.

OBJECT	LINE FLUX	3σ U. L.	EFF. EXP.
(x 10^{-5} photons/cm^2 s)		(days)	
Cyg X-1	1.24 ± 0.71	3.36	28.19
Cyg X-3	0.98 ± 0.71	3.10	25.91
2000 + 251	1.21 ± 0.71	3.33	25.75
2023 + 338	1.44 ± 0.71	3.57	26.55
LMC X-1	-1.84 ± 0.68	2.05	21.65
LMC X-3	-2.48 ± 0.67	2.01	20.27
CAL 83	-2.03 ± 0.67	2.01	21.74
GX 339-4	-1.48 ± 0.79	2.36	28.89
SS 433	-2.36 ± 0.71	2.12	25.85
Aql X-1	-1.69 ± 0.71	2.12	26.59
Cen X-3	-0.64 ± 0.75	2.24	23.61
N Mus 91	-1.30 ± 0.77	2.32	22.25
Her X-1	1.26 ± 0.89	3.93	10.22
0115 + 63	1.24 ± 0.82	3.71	13.05
Vela X-1	-1.47 ± 0.82	2.47	17.38
CAL 87	-2.64 ± 0.73	2.20	21.98
Sco X-1	-1.48 ± 0.97	2.90	27.46
0620 + 00	-0.08 ± 0.98	2.94	20.21
1755 - 338	-1.21 ± 0.91	2.74	36.19
Cir X-1	-2.14 ± 0.79	2.36	23.37

The X-ray binary 2023 + 331 had a likelihood ratio of 16.1, which formally corresponds to a 4σ detection (corresponding to a probability of 6 x 10^{-5} for it to be a random effect). In order to fully ascertain the significance of this measurement, we need to also consider the number of trials in this analysis. We have performed 60 independent trials (20 objects, 3 independent observations) looking for 2.2 MeV line emission. Taking this into account, the probabaility for a random effect is now .0086, corresponding to a significance level of just under 3σ. This therefore becomes a marginal detection.

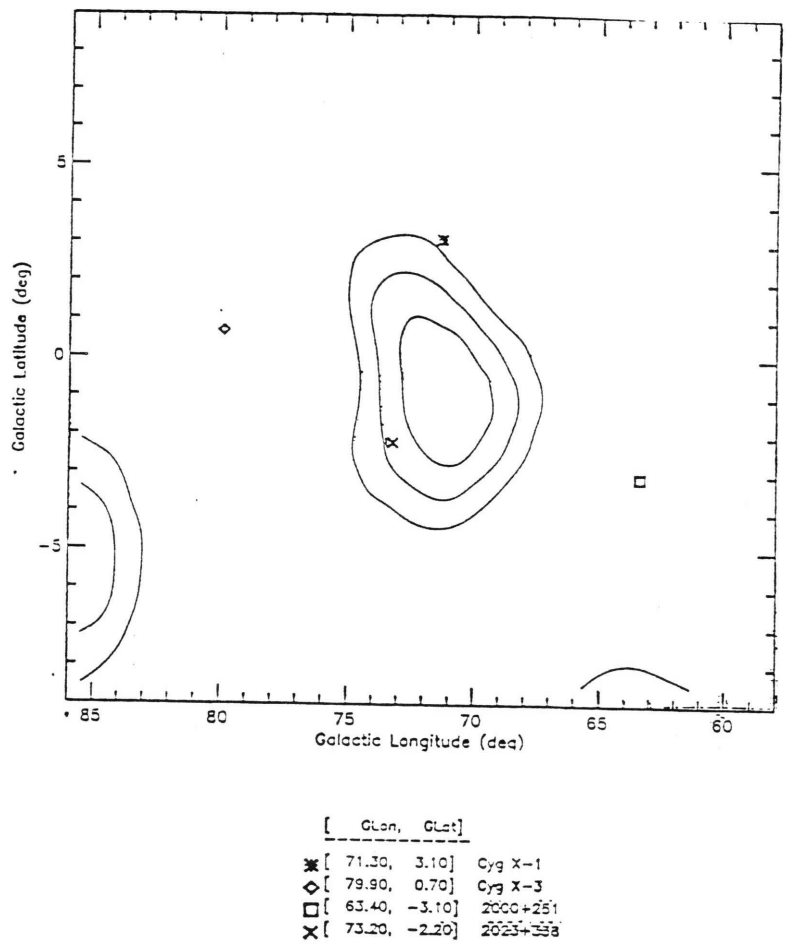

Figure 3.5. The maximum likelihood map for phase 2 data of the Cygnus region.

Aside from the marginal 2.2 MeV detection of 2023+338 in phase 2, the other flux values yield upper limits on the neutron capture line from X-ray binaries which are the most restrictive yet published. These improve the Cygnus X-1, Cygnus X-3 and Sco X-1 upper limits from the Solar Maximum Mission by an order of magnitude.

3.3 Phase-resolved Analysis of Cygnus X-1 and Cygnus X-3

In Sections 1.2.3 and 1.2.4 we discussed two general models for 2.2 MeV line emission, which would both exhibit flux variations as a function of orbital phase. Both of these theories have fluxes which are near the limit of COMPTEL's line sensitivity. Since we see no evidence of time-averaged 2.2 MeV line emission, we decided to search for line emission as a function of orbital phase. If there is orbital phase dependent emission, the COMPTEL line sensitivity will be improved by performing a phase-resolved analysis. If the signal is confined to a narrow phase interval, then restricting the analysis to that interval will reduce the background level considerably without reducing any of the signal. The signal to noise ratio is improveded and the sensitivity of the source measurement is increased.

3.3.1 Epoch-folding the COMPTEL Data

The first step in the orbital phase-resolved analysis was to re-accumulate all of the necessary COMPTEL data with respect to the desired range of orbital phase. Only viewing periods in which the source location was within 40 degrees of the COMPTEL pointing direction were used for the orbital phase analysis (see Tables 3.5 and 3.6). The orbital period was broken up into five equal time intervals, beginning with 0.0 - 0.2, for both Cygnus X-1 and Cygnus X-3.

3.3.2 Cygnus X-1 Results

The values for the orbital parameters were taken from Gies and Bolton (1982) where T_0 = JD 2,441,869.3 (where JD refers to Julian Day) and the orbital period P is 5.6 days. This is a linear fit where

$$T_n = T_o + n*P \qquad (3.1)$$

T_n is the epoch for the nth orbit, and n is some integer number. The viewing periods used in this study are listed in Table 3.5. The following figure is a plot of the line flux values and their associated 1σ error bars. As can be seen, the flux values are consistent with zero and there is no evidence of enhanced 2.2 MeV emission in any of the orbital phase intervals.

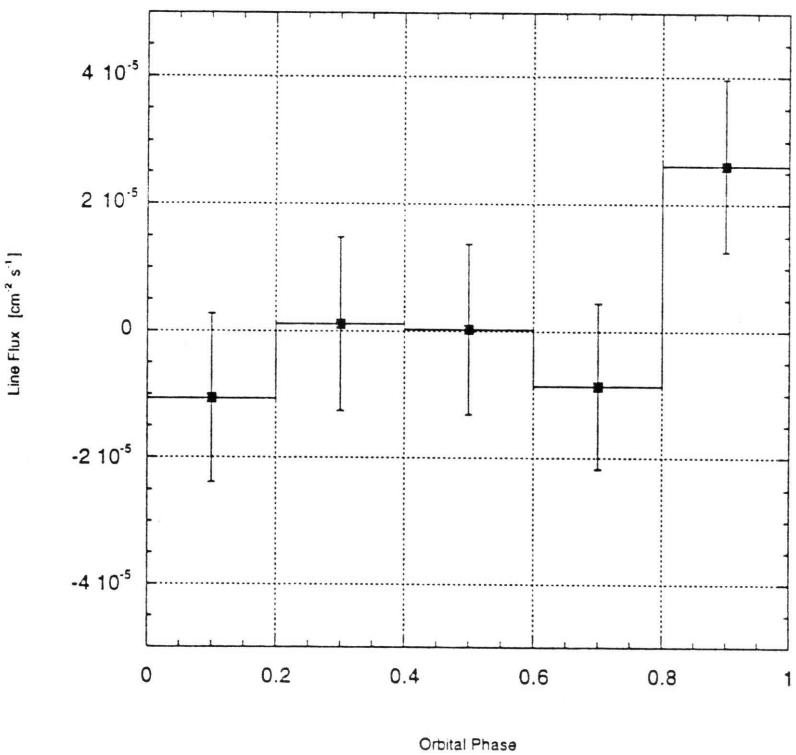

Figure 3.6. Line fluxes for Cygnus X-1 orbital phase-resolved emission.

Table 3.5. Viewing periods used for Cygnus X-1 orbital phase-resolved analysis.

VP	TARGET	*l* (deg)	*b* (deg)	Z.A. (deg)
2.0	Cyg X-1	73.0	3.0	1.7
7.0	Cyg X-3	70.0	-8.0	11.2
9.5	Her X-1	60.0	40.0	38.3
20.0	SS 433	40.0	1.0	31.3
34.0	CAS A	109.0	-2.0	38.0
201.0	Her X-1	67.0	39.0	36.1
202.0	Her X-1	71.0	40.0	6.9
203.0	Cyg X-3	78.0	1.0	7.0
203.3	Cyg X-3	78.0	1.0	7.0
203.6	Cyg X-3	78.0	1.0	7.0
212.0	WR 140	84.0	12.0	15.4
303.2	N Cyg 1992	89.0	8.0	18.3
303.7	N Cyg 1992	89.0	8.0	18.3
318.1	Cyg X-1	68.0	0.0	4.5
328.0	PSR 1951+32	65.0	0.0	7.0
331.0	PSR 1951+32	65.0	0.0	7.0
331.5	PSR 1951+32	65.0	0.0	7.0
333.0	PSR 1951+32	89.0	8.0	7.0

where Z.A. is the zenith angle which is the angle between the COMPTEL pointing direction and the source location.

3.3.3 Cygnus X-3 Results

The values for the orbital parameters were taken from van der Klis and Bonnet-Bidaud (1989). The cubic ephemeris was used because of the quality of the fit to the data and because it seems most consistent with recent OSSE Cygnus X-3 observations of the period (Steve Matz, private communication). The cubic ephemeris is written as

$$T_n = T_o + P_o\, n + c_o\, n^2 + d\, n^3 \tag{3.2}$$

where

$$c_o = \frac{P_o \dot{P}_o}{2} \tag{3.3}$$

and

$$d \sim \frac{\dot{P}_o \ddot{P}}{6} \quad . \tag{3.4}$$

These quantities are defined the same as in the previous section except in this case we have the addition of terms relating to the first and second derivatives of the orbital period. Van

der Klis and Bonnet-Bidaud (1989) warn that this term is necessary for calculating a correct ephemeris during and after 1992. Since the COMPASS task which bins the data according to the epoch only allows for a linear fit (3.1), ephemerides were calculated for the middle of each viewing period used in this part of the study. The linear fit was adequate for each 2-3 week observation. The viewing periods used in this Cygnus X-3 study are listed in Table 3.6. The beginning orbital ephemeris was JD 2,440,949.9013, P_o was 0.199 days, c_o was 2.18×10^{-10} and d was -2.89×10^{-15}. The following figure is a plot of the line flux values and their associated 1σ error bars. As seen in Figure 3.7, all the flux values are consistent with zero and there is no evidence of enhanced 2.2 MeV mission in the 0.4 - 0.6 orbital phase.

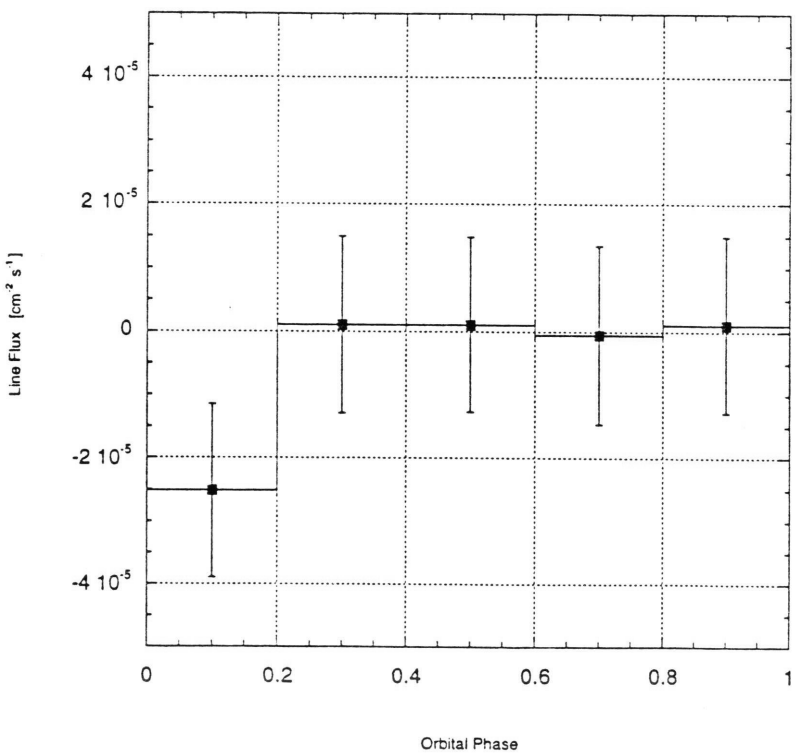

Figure 3.7. Line fluxes for Cygnus X-3 orbital phase-resolved emission.

Table 3.7. Viewing periods used for Cygnus X-3 orbital phase-resolved analysis.

VP	TARGET	l (deg)	b (deg)	Z.A. (deg)
2.0	Cyg X-1	73.0	3.0	7.3
7.0	Cyg X-3	70.0	-8.0	13.2
20.0	SS 433	40.0	1.0	39.9
34.0	CAS A	109.0	-2.0	29.2
203.0	Cyg X-3	78.0	1.0	1.9
203.3	Cyg X-3	78.0	1.0	1.9
203.6	Cyg X-3	78.0	1.0	1.9
212.0	WR 140	84.0	12.0	12.0
303.2	N Cyg 1992	89.0	8.0	11.6
303.7	N Cyg 1992	89.0	8.0	11.6
318.1	Cyg X-1	68.0	0.0	11.9
328.0	PSR 1951+32	65.0	0.0	14.9
331.0	PSR 1951+32	65.0	0.0	14.9
331.5	PSR 1951+32	65.0	0.0	14.9
333.0	PSR 1951+32	89.0	8.0	14.9

where Z.A. is the zenith angle which is the angle between the COMPTEL pointing direction and the source location.

CHAPTER IV
SUMMARY AND CONCLUSIONS

4.1 The Background Generation Methods

In our search for sources of unshifted 2.2 MeV gamma ray lines, we have examined three different background modeling procedures. The first modeling procedure had been used successfully in other GRO-COMPTEL studies and is based on smoothing the measured dataset in all three dimensions of COMPTEL's dataspace. The resulting model essentially removes (to first order) any sources from the dataspace. Since this method represents the default method for COMPTEL imaging, we have used this as a basis for comparison with other techniques. The drawback of this smoothing method for gamma ray line studies is that it results in images which are sensitive to all of the source flux (both line and continuum) within the energy range of the analysis. For the purposes of our study, we were more interested in an approach which was sensitive to line emission alone.

Considering COMPTEL's suitability as a gamma ray spectrometer (nuclear line sensitivity of an order of magnitude better than previous gamma ray experiments), several studies on gamma ray lines are presently on-going. These include the 1.8 MeV 26-Al line as supernovae tracers (Diehl *et al.*, 1995), potential lines from the Orion complex (Bloemen et al., 1994), as well as this search for the 2.2 MeV neutron capture line. As a result, many modeling procedures have been suggested specifically for gamma ray line imaging. But it should be noted that the study of 2.2 MeV lines from cosmic sources is complicated by an internally generated 2.2 MeV line, which neither of the other two projects mentioned above must overcome.

Our first attempt at modeling the background was based on COMPTEL simulations of this internally generated 2.2 MeV line. The idea was to model the 2.2 MeV line interval background as a sum of the dataspace distribution derived from simulations of the internal

2.2 MeV component and the (background) dataspace distribution derived from an adjacent energy band. In practice, however, this approach did not give consistent results for the 2.2 MeV line intensity when compared with that derived from the background energy spectrum. It was decided the background in this energy range was more complex than this modeling procedure would allow. For example, the inclusion of the instrumental sodium cascade lines should be considered in addition to more robust models of the continuum. In order to proceed with our studies, another approach was then examined.

This third modeling approach was based on independent modeling of the (χ,ψ) and the distributions. The distribution in (χ,ψ) was found to be energy independent (Knödelseder, 1994) and so the form of this distribution was taken from the energy interval from 1 to 10 MeV. This was subsequently combined with the $\bar{\phi}$ distribution as taken from the energy region centered on the 2.2 MeV line. This more empirical approach to modeling the background was then tested in three distinct ways.

Each of the three tests will be considered here. The first test was a null test to show that in the absence of any expected 2.2 MeV line sources, the background model would not create artificial sources. The Virgo region was chosen and imaged for four time intervals, the final time interval being the sum of the first three. In all four cases, this line background modeling procedure showed no evidence of 2.2 MeV line emission. The second test, using the same time intervals, was to image a region with a known, strong continuum source. Ideally, if the background is being modeled appropriately, then any continuum source would be removed in the final image. The Crab nebula/pulsar was selected as it is a very strong source of continuum MeV gamma rays in our energy range of interest. While the Crab was detected at high significance using the background model derived from the standard dataspace smoothing, it was effectively removed using the gamma ray line background. Although some residuals remained, the Crab signal was largely removed in this analysis. The third and final test was a verification that a signal from a 2.2 MeV line would be detected. The solar flare of June 11, 1991 was chosen since

it was well studied by the COMPTEL team (Rank 1996 and Suleiman 1995) and it had a strong 2.2 MeV line. Again, the smoothed background model and the line background model were compared. Both showed very high detection significances. More importantly, both techniques gave results for the 2.2 MeV fluence which were consistent with that derived directly from the flare energy spectrum. With these three tests passed, the line background model was considered appropriate to use to image the sky at 2.2 MeV.

4.2. All-Sky Maps Results

Unlike previous instruments, COMPTEL has been able to provide data suitable to the generation of all sky maps. This is because of COMPTEL's wide field of view and the fact that the first 15 months of its operation was used to survey the entire sky. The maximum entropy method was used to produce all sky maps for four time intervals, three mission phases and the sum of these phases (over 3 years of data). These maps represent the first-ever all-sky maps produced at the wavelength of 2.2 MeV gamma-rays.

Several interesting features seen in the maximum entropy maps were studied in more detail using a maximum likelihood analysis. Four features were found to have a formal significance of greater than 3σ. However, when some allowance is made for the number of trials in the analysis, none of these features exhibits a significance in excess of 3σ.

4.3 X-ray Binary Source Results

Twenty X-ray binaries were selected for a more quantitative study. Cygnus X-1 and Cygnus X-3 were included because they are the best candidates for detecting 2.2 MeV emission, due to their luminosity and their proximity. We also had two theories (see Section 4.1.2) which predicted 2.2 MeV line emission from these objects on the order of COMPTEL's line sensitivity. Scorpius X-1 was chosen because SMM and HEAO-3 had already published upper limits for this object and we would be able to improve on these

results. Because one theory predicted 2.2 MeV line fluxes for Cygnus X-1, other black hole candidates were chosen. Since the other theory depended on TeV emission, other objects from which TeV detections were claimed were also included in the search. The upper limits which we obtained represent an improvement upon previously published results by an order of magnitude for Cygnus X-1, Cygnus X-3 and Scorpius X-1. Additionally, we have given upper limits on many objects never before searched for 2.2 MeV line emission. It should also be noted that by examining the all-sky maps, all XRBs were sampled. Any not included on the target list but that showed up as repeating hot spots would then, in essence, added to the list of objects to be quantitatively studied. These results should serve to constrain the theoretical models.

The fact we did not see any evidence of 2.2 MeV line emission from either Cygnus X-1 and Cygnus X-3 does not dismiss either theory. A more crucial test of those theories will the orbital phase analysis, since both theories would show evidence of 2.2 MeV line emission which would vary as a function of orbital phase.

4.3 Orbital Phase-resolved Study

4.3.1 Cygnus X-1 Study

Guessoum and Dermer (1988) give a range of predicted values for the 2.2 MeV line flux from Cygnus X-1. These values are from 2.8 x 10^{-6} cm^{-2} s^{-1} to 3.4 x 10^{-5} cm^{-2} s^{-1} and are dependent on two parameters. Firstly, the initial ion temperature of the plasma and secondly the ratio of 2.2 MeV photons escaping from the companion star to the number of neutrons escaping the plasma. As the initial ion temperature increases from 5 MeV to 20 MeV, so does the predicted line flux. If the initial ion temperature is greater than 20 MeV, then the predicted flux begins to decrease. The observed flux is inversely proportional to the second parameter, reflecting the production (or lack therefore) of 2.2 MeV photons as a function of the number of neutrons escaping the hot accretion region. Also, the 2.2 MeV line emission would vary with orbital phase.

Our results from the first three years of operation show line fluxes for Cygnus X-1 which are all consistent with zero within 3σ. The orbital phase-averaged 3σ upper limit was 2.6 x 10^{-5} cm^{-2} s^{-1}, an order of magnitude improvement over SMM results (Harris & Share, 1991). Our orbital phase-resolved analysis over the same time interval also showed line fluxes all consistent with zero. There was no evidence of enhanced emission during any of the orbital phases or mission phases.

While these results cannot rule out the possibility of a two temperature plasma, they do constrain the theoretical model. The range of acceptable initial ion temperatures is then under 5 MeV or above 50 MeV if we do not vary the ratio of 2.2 MeV photons to escaping neutrons. Perhaps that the initial ion temperature is sufficient to create the energies required for 2.2 MeV line production in X-ray binaries, but the number of neutrons leaving and imparting on the companion star is not currently measurable.

4.3.2 Cygnus X-3 Study

Vestrand (1990) gives an estimate of the 2.2 MeV peak line flux for Cygnus X-3 to be 2.0 x 10^{-4} cm^{-2} s^{-1} (1.6). The estimate also depends on the fraction of energetic neutrons which thermalize and decay, the solid angle subtended by the companion star, the proton luminosity and the distance to Cygnus X-3. The production of neutrons are dependent on the production of an energetic proton beam. As evidence that the beam is on, one would expect to see TeV emission, depending on the orbital geometry of the beam and the observer. Additionally, this theory predicts line emission which would vary with respect to orbital phase.

COMPTEL results from the first three years of operation show line fluxes for Cygnus X-3 which are all consistent with zero within 3σ. The overall 3σ upper limit was 2.4 x 10^{-5} cm^{-2} s^{-1}, again an order of magnitude improvement over SMM. Our orbital phase-resolved analysis using the same data also showed line fluxes all consistent with zero. No enhanced emission was seen during any orbital phase.

These results cannot discount the possibility of a neutron capture line resulting from the TeV energetic protons. While the 3σ upper limit is much lower than Vestrand's predicted emission, there have been no recent reports of TeV emission from Cygnus X-3, which means that there is no evidence that the energetic proton beam was on. Therefore, our ability to estimate the proton luminosity, necessary to test Vestrand's 2.2 MeV line flux limits, is hampered. If we can assume that the energetic proton beam was on, we can say one of two things. The average neutron energy was too high so 2.2 MeV line production happened too deep into the companion star's atmosphere to escape as 2.2 MeV line emission. Or the proton luminosity should be either 10^{38} ergs or lower.

4.4 Future Work

While COMPTEL data has been able to generate all sky maps as well as place the most restrictive upper limits on 2.2 MeV line emission from selected X-ray binaries, additional work can be done on this project. COMPTEL has continued to collect data from target specific observations from October 1994 onwards. Inclusion of these additional data would improve COMPTEL's line sensitivity. In addition, improvements in background modeling may still be possible. For example, one question which remains is the residual emission of the Crab pulsar, which remains after the application of the background model. Further investigation of this issue would be helpful. Also, there are several other background modeling procedures for the COMPTEL instrument. This procedures ought to be tested using the same three test process (null test of the Virgo region, Crab continuum test and June 11, 1991 solar flare positive signal test) as was the background model process we used. Thus, we can expect improvements both in sensitivity (via more observation time) and in the data analysis (via the background modeling). It may still be possible that, at some point in the future, COMPTEL may be able to detect a positive 2.2 MeV signal from some cosmic source.

REFERENCES

Aharonian, F.A. & Sunyaev, R.A. 1984 *MNRAS* **210**, 257

Bhattacharya, D *et al. BAAS* **22**, 1229

Bonnet-Bidaud, J-M. & Chardin, G. 1988 *Phys. Rep.* **170**, 325

Bloemen, H. *et al.* 1993, *Astrophys.J. Suppl. Ser.* **92**, 419

Bloemen, H. *et al.* 1994, *Astron.Astrophys.* **281**, L5

Bowers, R. & Deeming, T. 1984, *Astrophysics 1:Stars* (Boston: Jones & Bartlett)

de Boër, H. *et al.* 1991 in *Data Analysis in Astronomy IV*, ed. V. Di Gesù, *et al.* (New York: Plenum Press) Vol 59, p 241

Diehl, R. *et al.* 1995, *Astron.Astrophys.* **298**, 445

Guessoum, N. and Dermer, C. 1988 in *AIP Conf.Proc. No. 170, Nuclear Spectrosocopy of Astrophysical Sources*, ed. N. Gerhels & G. Share (New York:AIP Press) p 332-337

Harris, M.J. & Share, G.H. 1991 *Astrophys.J.* **381**, 439

Higdon, J.C. & Lingenfelter, R.E. 1977 *Astrophys.J.* **215**, L53

Hua, X. & Lingenfelter, R.E. 1987 *Astrophys.J.* **323**, 779

Jacobson, A.S. *et al.* 1978 in *Gamma Ray Spectroscopy in Astrophysics*, ed. T.L. Cline & R. Ramaty (Washington: NASA) p 228

Johnson, W.N. *et al.* 1989 in *Proc. of the Gamma Ray Observatory Science Workshop*, ed. W.N. Johnson (Washington: NASA)

Knödelseder, J. 1994, *Diplom Thesis*, MPE Garching, Germany

Lingenfelter, R.E. et al, 1978 in *Gamma Ray Spectroscopy in Astrophysics*, ed. T.L. Cline & R. Ramaty (Washington: NASA) p 252

Lingenfelter, R.E. & Ramaty, R. 1978 *Physics Today* **31**, 40

Longair, Malcolm S. 1994 *High Energy Astrophysics Volume 2*, second ed. (Cambridge: Cambridge University Press)

Miller, J.A. & Viñas, A. 1993 *Astrophys.J.* **412**, 386

Miyosji, M. *et al.* 1995 *Nature* **373**, 127

Murphy, R.J. & Ramaty, R. 1985 *Adv. Space Res.* **4**(7), 127

Murphy, R.J. *et al.* 1991 *Astrophys.J.* **371**, 793

Ramaty, R. & Lingenfelter, R.E. 1995, in *The Analysis of Emission Lines*, ed. R.E. Williams & M. Livio (Cambridge: Cambridge University Press) (in press)

Rank, Gerhard 1995 *Ph.D. Dissertation*, MPE Garching, Germany (in press)

Schönfelder, V. *et al.* 1993, *Astrophys.J. Suppl. Ser.* **86**, 657

Shapiro, S.L. & Teukolsky, S.A. 1983 *Black Holes, White Dwarfs and Neutron Stars* (New York: John Wiley & Sons)

Shapiro, S.L., Lightman, A.P. & Eardley, D.M. 1976 *Astrophys.J.* **204**, 187

Shu, Frank 1982 *The Physical Universe* (Mill Valley: University Science Books)

Stacy, G. *et al.* 1995 in *AIP Conf. Proc., Third Compton Symposium* , (New York: AIP Press) (in press)

Strong, A. *et al.* 1991 in *Data Analysis in Astronomy IV*, ed. V. Di Gesù, *et al.* (New York: Plenum Press) Vol 59, p 251

Suleiman, Raid 1995 *Master's Thesis*, University of New Hampshire, Durham, NH

Tanaka, Y & Lewin, W.H.G. 1995 in *X-ray Binaries* ed. W.H.G. Lewin, J. van Paradijs & E.P.J. van den Heuvel (Cambridge: Cambridge University Press)

Vacanti, G. *et al.* 1991 *Astrophys.J.* **377**, 467

van Paradijs, J. 1995 in *X-ray Binaries* ed. W.H.G. Lewin, J. van Paradijs & E.P.J. van den Heuvel (Cambridge: Cambridge University Press)

Vestrand, W. T. 1990 *Astrophys.J.* **352**, 353

Wang, H.T. & Ramaty, R. 1974 *Solar Phys.* **36**, 129

Weekes, Trevor C. 1992 *Space Sci.Rev.* **59**, 315

Weidenspointer, G. 1994 *Diplom Thesis*, MPE Garching, Germany

Winkler, C. *et al.* 1992 *Astron.Astrophys.* **255**, L9

White, N.E. *et al.* 1995 in *X-ray Binaries* ed. W.H.G. Lewin, J. van Paradijs & E.P.J. van den Heuvel (Cambridge: Cambridge University Press)

Zel'dovich, Ya.B. & Guseynov, O.H. 1965 *Astrophys.J.* **144**, 840